Check for updates

ChemSusChem

Review
doi.org/10.1002/cssc.202400663

Chemistry Europe
European Chemical Societies Publishing

www.chemsuschem.org

Interfacial Design of Particulate Photocatalyst Materials for Green Hydrogen Production

Tomohiro Higashi[a] and Kazunari Domen*[b, c, d]

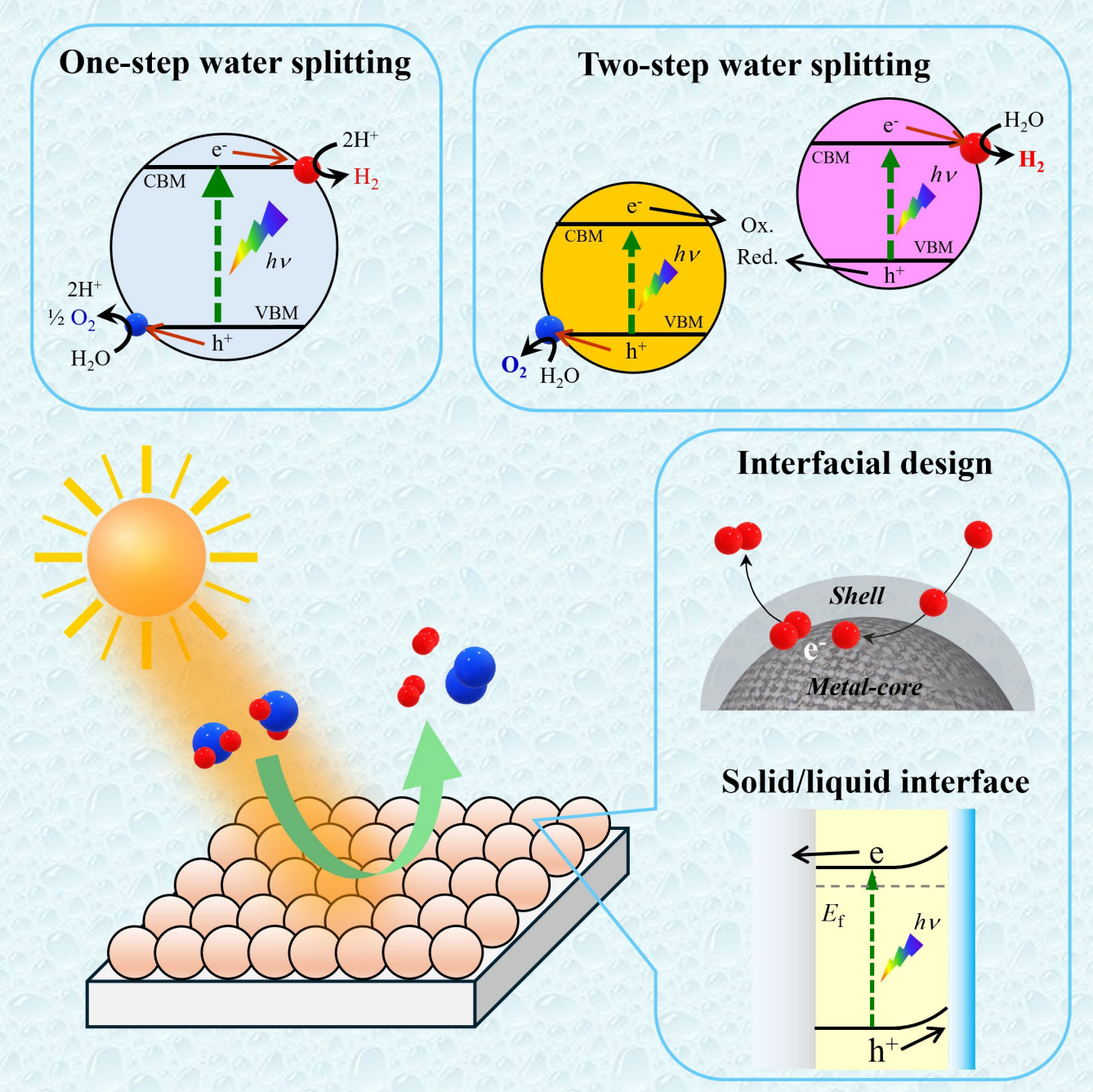

© 2024 The Authors. ChemSusChem published by Wiley-VCH GmbH

Green hydrogen production using particulate photocatalyst materials has attracted much attention in recent years because this process could potentially lead to inexpensive and scalable solar-to-chemical energy conversion systems. Although the development of efficient particulate photocatalysts enabling one-step overall water splitting (OWS) with solar-to-hydrogen efficiencies in excess of 10% remains challenging, promising photocatalyst candidates exhibiting OWS activity have been demonstrated. This review provides a comprehensive introduction to the solar-to-hydrogen energy conversion process of semiconductor photocatalyst materials and highlights recent advances in photocatalytic OWS via both one-step and two-step photoexcitation processes. The review also covers recent developments in the photocatalytic OWS of $SrTiO_3$, including the establishment of large-scale photocatalytic systems, interfacial design using cocatalysts to enhance water splitting activity, and its photoelectrochemical (PEC) properties at the electrified solid/liquid interface. In addition, there is a special focus on visible-light-absorbing oxynitride and oxysulfide particulate photocatalysts with absorption edges near 600 nm. Methods for photocatalyst preparation and surface modification, as well as PEC properties, are also discussed. The semiconductor properties of particulate photocatalysts obtained from photoelectroanalytical evaluations using particulate photoelectrodes are evaluated. This review is intended to provide guidelines for the future development of particulate photocatalysts capable of efficient and stable OWS.

1. Introduction

Green hydrogen production is a promising means of generating a renewable source of energy that can be both stored and transported.[1] The use of fossil fuels such as oil, coal and natural gas for energy is presently depleting limited reserves of such materials and also producing environmental impacts, notably carbon dioxide emissions from combustion. In contrast, the combustion of hydrogen with oxygen gives only water, thereby providing a carbon-neutral and emission-free cycle. Among the various approaches to green hydrogen production, photocatalytic water splitting using solar energy derived from sunlight and water is of particular interest. This eco-friendly method is currently viewed as an ideal energy conversion technology that may realize a sustainable hydrogen-based society in future.

To date, various water splitting systems using semiconductor photocatalysts or photoelectrodes have been proposed.[2] Upon exposure to light, electrons and holes are generated inside semiconductor photocatalysts and subsequently migrate to reaction sites at the solid/liquid interface. Hydrogen and oxygen are then generated via water reduction and oxidation reactions, respectively. In systems using powdered photocatalysts, the water splitting reaction is induced by irradiating photocatalyst particles suspended in water with sunlight. Investigations into water splitting that instead employ photocatalyst sheets or large-scale panels immobilized on substrates are also underway.[3] Interestingly, powder-based particulate photocatalysts could allow the construct of solar-powered hydrogen production systems without the need for complicated equipment.

Since the discovery of the Honda-Fujishima effect in 1972, TiO_2 has been extensively investigated as a promising catalyst for photocatalytic and photoelectrochemical (PEC) water splitting.[4] Initially, TiO_2 single crystals were used to fabricate photoelectrodes for PEC systems and such systems became one of the most thoroughly studied solar-to-chemical conversion processes, with applications including environmental purification.[5] Although the application of an external bias is required to drive the water splitting reaction in these systems, this semiconducting material was found to be capable of converting solar energy into chemical energy in the form of hydrogen. Overall water splitting (OWS) using TiO_2 and $SrTiO_3$ as particulate photocatalysts suspended in water was subsequently reported in 1980.[6] However, these compounds were only able to absorb ultraviolet (UV) radiation. Thereafter, a variety of particulate semiconductor materials were investigated for applications in non-biased OWS as well as other artificial photosynthetic reactions.[7] Such research has focused on the development of visible-light-responsive particulate photocatalysts enabling sunlight-driven non-biased OWS.

In the case of PEC water splitting, single-crystal semiconductors as well as thin films and assemblies of particles have been utilized to fabricate photoelectrodes. These electrodes are subsequently connected to an external electrical circuit to control the photoelectrode potential at the solid/liquid interface.[8] In the case that such photoelectrodes are immersed in an aqueous solution, band bending typically occurs at the solid/liquid interface and photoelectrodes consisting of p-type and n-type semiconductors can be used for the hydrogen evolution reaction (HER) and oxygen evolution reaction (OER), respectively.[9] Based on controlling the potential of the photoelectrode during exposure to light, PEC water splitting can be induced at photoelectrode potentials higher and lower than the standard redox potentials for the HER and OER, respectively.

[a] Dr. T. Higashi
Institute for Tenure Track Promotion, University of Miyazaki
1-1 Gakuen-Kibanadai-Nishi, Miyazaki 889-2192, Japan
[b] Prof. Dr. K. Domen
Office of University Professors, The University of Tokyo
2-11-16 Yayoi, Bunkyo-ku, Tokyo 113-8656, Japan
E-mail: domen@chemsys.t.u-tokyo.ac.jp
[c] Prof. Dr. K. Domen
Research Initiative for Supra-Materials, Interdisciplinary Cluster for Cutting Edge Research, Shinshu University
4-17-1 Wakasato, Nagano 380-8533, Japan
[d] Prof. Dr. K. Domen
Department of Chemistry, Kyung Hee University
Seoul, 130–701, Republic of Korea

© 2024 The Authors. ChemSusChem published by Wiley-VCH GmbH. This is an open access article under the terms of the Creative Commons Attribution Non-Commercial License, which permits use, distribution and reproduction in any medium, provided the original work is properly cited and is not used for commercial purposes.

1864564x, 2024, 21, Downloaded from https://chemistry-europe.onlinelibrary.wiley.com/doi/10.1002/cssc.202400663 by Turkey Cochrane Evidence Aid, Wiley Online Library on [04/09/2026]. See the Terms and Conditions (https://onlinelibrary.wiley.com/terms-and-conditions) on Wiley Online Library for rules of use; OA articles are governed by the applicable Creative Commons License

The magnitude of the resulting photocurrent density generated by the photoelectrodes and the position of the onset potential are regarded as indicators of PEC performance. A PEC system can also be used to quantitatively evaluate the intrinsic characteristics of semiconductors and the activity of photocatalyst materials. Such information can provide design strategies that may be used to improve the activity of particulate photocatalyst materials.

The solar-to-hydrogen (STH) energy conversion efficiency obtainable from a catalyst greatly depends on the optical properties (such as bandgap energy) and band position for the material relative to the standard water redox potential, with values of 0.0 V vs. reversible hydrogen electrode (V_{RHE}) for the HER and 1.23 V_{RHE} for the OER.[10] Based on the thermodynamic requirements associated with non-biased OWS, the conduction band minimum (CBM) and valence band maximum (VBM) for the photocatalyst must straddle the standard redox potentials of the HER and OER regardless of the pH of the aqueous solution.[1c] The solar spectrum comprises large proportions of visible and infrared light, such that the STH energy conversion efficiency for a photocatalytic water splitting system is limited by the bandgap energy of the photocatalyst. Typical oxide photocatalysts such as TiO_2 and $SrTiO_3$ have bandgap energies on the order of 3.0 eV and can therefore absorb only the UV region of sunlight. Consequently, these materials cannot provide the STH efficiency values of at least 10% required for practical applications. A semiconductor photocatalyst having a bandgap energy of less than approximately 2.9 eV (meaning an absorption edge wavelength longer than 420 nm) would be preferable with regard to the efficient absorption of solar radiation in the visible region. Ta_3N_5 is an example of a visible-light-responsive narrow-bandgap photocatalyst capable of light absorption at wavelengths up to 600 nm, equivalent to a bandgap energy of 2.1 eV.[11] The theoretical STH energy conversion efficiency obtainable for this bandgap is 15.26% assuming a quantum yield of 100% under 1 sun illumination.[12] Thus, the development of efficient semiconductor photocatalysts with longer absorption edge wavelengths, preferably on the order of 600 nm, will be required to obtain STH efficiencies sufficient for commercial applications.

This review article examines recent efforts to develop particulate photocatalyst materials applicable to OWS. The practical implementation of green hydrogen production hinges on the ability to capture light over wide areas and to utilize radiation having a broad range of wavelengths for photocatalytic water splitting. Thus, the latest progress in visible-light-responsive particulate photocatalyst materials such as (oxy)nitrides and (oxy)sulfides is summarized. The surface modification of photocatalysts with cocatalysts and rational interfacial design guidelines for catalytic reaction sites promoting the HER and OER are also examined herein. The PEC characteristics of particulate photocatalysts have been found to correlate with the semiconductor properties at the electrified solid/liquid interface, which in turn are affected by the photoelectrode potential. As such, these factors are considered. Finally, this article describes work to date regarding the development of efficient visible-light-driven photocatalytic water splitting systems and issues limiting the water splitting efficiency, together with possible future developments. Readers who are interested in the cost and efficiency targets of solar-to-fuel conversion systems operating on a practical scale are encouraged to refer to other publications.[1e,2b,13]

2. Principles of Photocatalytic Water Splitting

In this section, the principles of photocatalytic water splitting to produce hydrogen and oxygen are briefly summarized. Solar-to-chemical energy conversion, such as the generation of green hydrogen via water splitting over a semiconductor photocatalyst, is based on six different processes. These are I) photon absorption, II) excitation separation, III) carrier diffusion, IV) carrier transport, V) efficient catalysis, and VI) mass transfer of reactants and products.[2a] Figure 1 provides a series of diagrams that summarize these processes and the corresponding time-scales on which they occur. It should be noted that processes III and IV can occur simultaneously. To achieve efficient photocatalytic OWS, all these processes (which are related to the physicochemical characteristics of the photocatalytic materials being used and occur on different time scales) must be optimized. This so-called six-gear concept was first proposed by Takanabe in 2017 as a means of enabling a comprehensive and quantitative discussion of each of these processes[2a] and this concept has been described at length in various publications.[14]

If all processes from light absorption (step I) to mass transfer (step VI) are highly efficient and do not undergo deactivation,



Tomohiro Higashi received a Ph. D. degree in engineering from Nagasaki University under Prof. Sagara's supervision in March 2015. After graduation, he joined The University of Tokyo and was appointed a postdoc researcher in April 2015 and a project assistant professor in 2017. He moved to University of Miyazaki as assistant professor (PI) in November 2021. His major research interests are the development of photoelectrochemical devices and the electroanalytical chemistry for semiconductor-based photocatalyst/photoelectrode materials.



Kazunari Domen received a Ph.D. degree in chemistry from The University of Tokyo in 1982. He joined the Chemical Resources Laboratory, Tokyo Institute of Technology, in 1982 as an assistant professor and was promoted to an associate professor in 1990 and professor in 1996. He moved to the University of Tokyo as a professor in 2004. He was cross appointed to Shinshu University, as a special contract professor in 2017. He is a university professor in The University of Tokyo, since 2019. He has been working on overall water splitting reaction on particulate photocatalysts to generate solar hydrogen.

© 2024 The Authors. ChemSusChem published by Wiley-VCH GmbH

1864564x, 2024, 21, Downloaded from https://chemistry-europe.onlinelibrary.wiley.com/doi/10.1002/cssc.202400663 by Turkey Cochrane Evidence Aid, Wiley Online Library on [04/09/2026]. See the Terms and Conditions (https://onlinelibrary.wiley.com/terms-and-conditions) on Wiley Online Library for rules of use; OA articles are governed by the applicable Creative Commons License

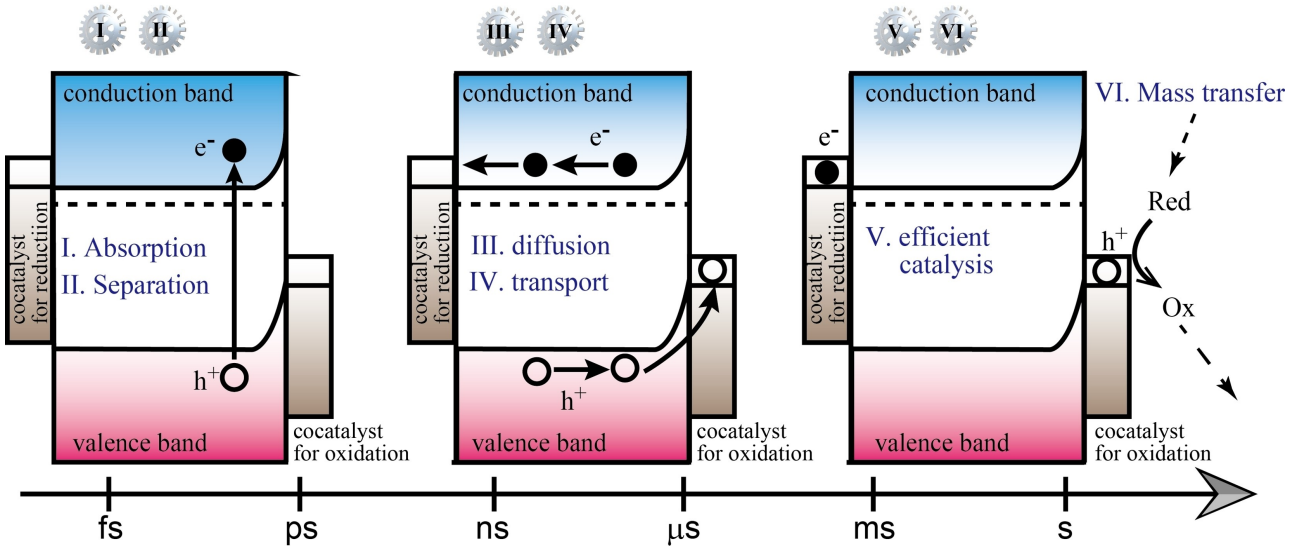

Figure 1. Diagrams portraying the photocatalytic processes associated with redox reactions such as water splitting that occur on different time scales. The Roman numerals above the images indicate the order in which these processes must occur to ensure overall water splitting.

the overall photocatalytic water splitting efficiency will naturally increase. In particular, the catalytic efficiency (step V) is governed by the performance of one or more cocatalysts loaded on the surface of the semiconductor photocatalyst. The extent to which the cocatalyst improves efficiency is, in turn, determined by electrocatalytic parameters such as the overpotential and chemical stability at the electrified solid/liquid interface. Consequently, the development of advanced designs for the solid/liquid interface will be a necessary prerequisite to accomplishing an efficient photocatalytic reaction. As part of this design process, the absorption and reflection of incident radiation by the cocatalyst should be minimized to ensure that the semiconductor photocatalysts receive sufficient light. The metal- and metal-oxide-based nanoparticles are commonly loaded on the surface of particulate photocatalysts. The nanoparticle-based cocatalyst provides the catalytic site for water splitting to enhance the water splitting efficiency, in similar to the electrocatalyst. The development of an efficient cocatalyst is also crucial for improving the photocatalytic activity.

Water splitting reactions using photocatalytic particles are typically based on either one-step or two-step excitation.[10] In the following sections, the thermodynamic requirements for these processes are summarized. Following this, the concepts of photocatalytic sheets that promote a two-step excitation process and of PEC cells made with a combination of p-type and n-type semiconductor photoelectrodes are presented. Surface modification methods and cocatalysts promoting the OWS are also described.

2.1. Water Splitting using Particulate Photocatalysts

A particulate photocatalyst capable of splitting water into hydrogen and oxygen while suspended in water in response to light exposure could allow large-scale and cost-effective hydrogen production. Such systems would be simple and relatively easy to mass produce. Photocatalytic water splitting is driven by the electrochemical potential difference of the photocatalyst between the hydrogen and oxygen evolution catalytic sites.

Figure 2a depicts a one-step OWS system using a particulate photocatalyst loaded with HER and OER cocatalysts. Photogenerated carriers (electrons and holes) inside the photocatalyst migrate to the cocatalyst/water interface such that OWS proceeds. A conventional PEC process employs an aqueous solution having a high concentration of a salt serving as an electrolyte. This salt compensates for electrical losses related to the conductivity of the PEC system. Conversely, in the case of photocatalytic OWS, the OWS reaction can proceed in pure water without the need for electrolytes. In such systems, hydrogen and oxygen evolution sites on the photocatalyst particles are presumably in close proximity, meaning that H^+ ions produced by the OER and OH^- ions generated by the self-dissociation of water can provide conductivity between the reaction sites.[15] Because both hydrogen and oxygen can be generated at different locations on the same photocatalyst particle, a one-step OWS photocatalyst can be considered to comprise a nano-scale ensemble of PEC devices. However, the submicron size of photocatalyst particles complicates the spatial isolation of individual catalytic sites and the quantitative assessment of local activity. Recently, Askarova et al. succeeded in directly quantifying the intrinsic kinetics of HER and OER (stoichiometric H_2 and O_2 generation) on micrometer-sized single particles using photo-scanning electrochemical microscopy (photo-SECM),[16] providing the first demonstration that one-step OWS occurs within a single particle. Further improvements in probe tip resolution are expected to allow quantitative evaluation of the OWS system at the nanometer scale.

Figure 2b provides a diagram summarizing two-step OWS using two different particulate photocatalysts in the presence of an electron mediator. Such systems employ two kinds of

© 2024 The Authors. ChemSusChem published by Wiley-VCH GmbH

1864564x, 2024, 21, Downloaded from https://chemistry-europe.onlinelibrary.wiley.com/doi/10.1002/cssc.202400663 by Turkey Cochrane Evidence Aid, Wiley Online Library on [04/09/2026]. See the Terms and Conditions (https://onlinelibrary.wiley.com/terms-and-conditions) on Wiley Online Library for rules of use; OA articles are governed by the applicable Creative Commons License

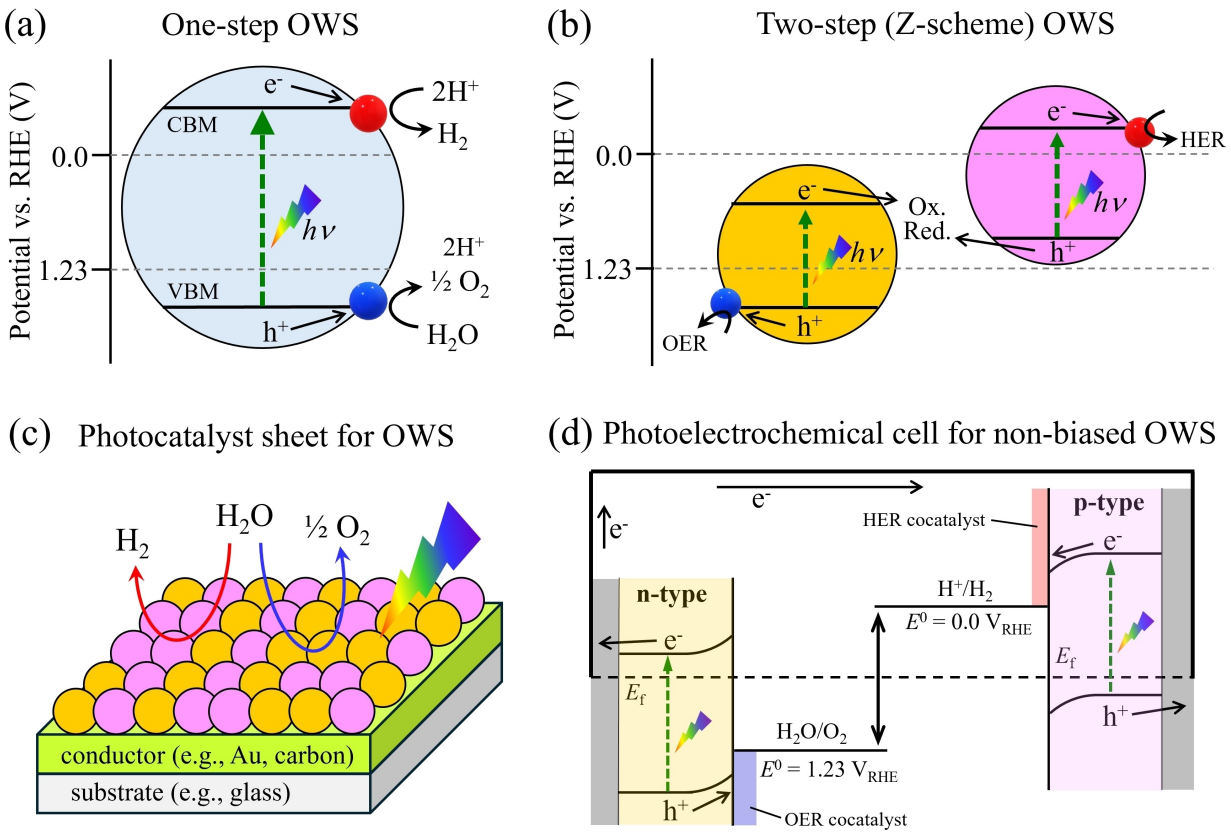

Figure 2. The basic principles of photocatalytic water splitting. Overall water splitting (OWS) by (a) one-step photoexcitation and (b) Z-scheme two-step photoexcitation. The red and blue spheres indicate cocatalysts for the hydrogen evolution reaction (HER) and oxygen evolution reaction (OER), respectively. (c) A depiction of OWS on a photocatalyst sheet comprising hydrogen evolution reaction (HER) and oxygen evolution reaction (OER) photocatalysts embedded in a conductive layer made of a material such as Au or C. This layer collects photogenerated charge carriers (electrons and holes) produced in response to light. (d) Energy level transitions occurring during non-biased OWS in a photoelectrochemical cell comprising a p-type semiconductor-based photocathode for the HER and an n-type semiconductor-based photoanode for the OER. E_f is the fermi level (photoelectrode potential) of the photoelectrodes when connected in series and exposed to light.

photocatalysts, one for the HER and one for the OER.[2c] This two-step OWS process is based on the Z-scheme electron relay, in which a mediator having an appropriate redox potential facilitates the transfer of charge carriers between the two photocatalysts.[10] This two-step OWS (Z-scheme) process can lower the thermodynamic requirements for water splitting, such as the required positions of the CBM and VBM. Electrons from the CBM of the photocatalyst (in the case of the OER) and holes from the VBM (in the case of the HER) recombine via a dissolved or solid electron mediator capable of undergoing a reversible redox reaction. Notably, photocatalysts capable of promoting either the HER or OER are applicable to two-step OWS.[15a] This represents an advantage of the Z-scheme system because various narrow-bandgap particulate photocatalysts can be combined to achieve OWS.

Figure 2c provides an illustration of a photocatalyst sheet intended for two-step OWS. In this system, particulate HER and OER photocatalysts are homogeneously dispersed and immobilized on a conductive substrate made of a material such as Au or C in close to proximity to one another.[17] Both p-type and n-type semiconductor photocatalysts have typically been employed as the HER and OER components, respectively, in photocatalyst sheets. The conductor serves as a carrier collection layer and provides charge recombination centers for electrons (from the n-type material) and holes (from the p-type material), similar to the role of the mediator in Z-scheme OWS. The photocatalyst sheet as shown here can allow efficient charge transfer between the two photocatalysts while also reducing solution resistance associated with the H^+/OH^- concentration overpotential.[15a] In principle, photocatalyst sheets could be scaled up without losing their inherent activity, even without the addition of a supporting electrolyte and connection through conductive wiring.

Figure 2d shows the mechanism associated with a typical PEC cell composed of a p-type semiconductor photocathode for the HER and an n-type semiconductor photoanode for the OER connected via a conductive wire. A PEC cell can decompose water into hydrogen and oxygen upon exposure to light without the application of an external bias voltage,[1b,9a] similar to the working principle of Z-scheme OWS on a photocatalyst sheet. In the case of a one-step water splitting system, the CBM and VBM of the semiconductor material must span the standard redox potentials for the HER and OER. A non-biased PEC cell functions via two-step photoexcitation, meaning that non-biased OWS can proceed. Consequently, the choice of photocatalytic semiconductor materials for water splitting can

© 2024 The Authors. ChemSusChem published by Wiley-VCH GmbH

1864564x, 2024, 21, Downloaded from https://chemistry-europe.onlinelibrary.wiley.com/doi/10.1002/cssc.202400663 by Turkey Cochrane Evidence Aid, Wiley Online Library on [04/09/2026]. See the Terms and Conditions (https://onlinelibrary.wiley.com/terms-and-conditions) on Wiley Online Library for rules of use; OA articles are governed by the applicable Creative Commons License

be greatly expanded. However, since a PEC system must incorporate an aqueous electrolyte solution (that is, a supporting electrolyte salt), this process is inferior to photocatalytic OWS in terms of scalability.[15c] Nevertheless, the photoelectrodes (photocathodes and photoanodes) in PEC system can be used to support the design and characterization of photocatalytic materials, because the properties of the photoelectrode at the solid/liquid interface can be analyzed as a function of electrode potential. Comprehensive studies involving photocatalysts and photoelectrodes conducted in this manner are likely to provide design strategies for the development of efficient solar-to-chemical conversion systems.

2.2. Particulate Photoelectrodes for the Evaluation of Physicochemical Properties at Solid/Liquid Interfaces

Photocatalysts intended for water splitting are commonly evaluated by assessing photocatalytic activity (as reflected by gas production, quantum efficiency and wavelength dependence). In particular, guidelines for the design of materials and surface modification can be obtained by evaluating particulate semiconductor photocatalysts at the solid/liquid interface. Qualitative assessments of intrinsic semiconductor properties can be performed by fabricating and characterizing particulate photoelectrodes at various electrode potentials.

When fabricating a semiconductor photoelectrode, it is vital that the semiconductor material exhibits excellent crystallinity and establishes intimate contact with the conductive substrate, offering low electrical resistance and minimal rectification. When these compounds are employed in the form of thin films, the range of applicable material systems is significantly restricted because the corresponding substrate must have a crystal structure suitable for thin-film formation to ensure stable, efficient electrical contact even under rigorous film formation conditions.[18] The production of particulate-based electrodes from powders has been assessed as an approach to mitigating challenges associated with the preparation of photoelectrodes from materials unsuitable for thin-film processes or to achieve large-area electrodes at reduced costs.[19]

Figure 3 summarizes typical methods for the fabrication of particulate photoelectrodes. Both electrophoretic deposition (Figure 3a, EPD)[20] and the doctor blade method (Figure 3b), which is similar to the squeegee method,[21] are commonly used to fabricate photoelectrodes from photocatalyst particles. In the EPD technique, photocatalytic particles are dispersed in a suitable solvent (such as acetone or ethanol) following which conductive electrodes made of materials such as indium tin oxide (ITO) or fluorine-doped tin oxide (FTO) are immersed on opposite sides of the dispersion. An external bias voltage is applied to these electrodes such that particles migrate to the substrate. After depositing the particles, necking or heat treatment is used to electrically bond the particles to the conductive substrate as well as to ensure contact between the particles.[20a] The resulting specimens can be used for PEC trials. In the case of the doctor blade method (Figure 3b), an ink is prepared from the particles and is dropped onto the substrate; the particles are immobilized while moving the blade to achieve the desired film thickness. Although the thickness and surface structure of the resulting particulate photoelectrode will vary depending on the distance between the blade and the substrate and the rate of movement, this method can produce electrodes with good reproducibility. Samples prepared using the doctor-blade method can be used to evaluate optical properties of the particles such as light transmittance.

Figure 3c summarizes the use of the particle-transfer method to create high-quality particulate photoelectrodes.[22] Briefly, photocatalyst particles are deposited on a substrate made of a material such as glass via drop-casting or spraying to form multiple layers, after which the specimen is transferred into a vacuum chamber. A metal back contact layer is subsequently deposited on the top surface of the multilayer using thermal evaporation, magnetron sputtering or chemical vapor deposition.[23] Following this, the metal/particle film assembly is lifted off the glass substrate using double-sided carbon adhesive tape and the specimen is sonicated in ultrapure water to remove excess loosely attached particles. The resulting assembly can be employed as a particulate photoelectrode by creating an electrical contact using a lead wire. If the crystallinity of the particles is sufficiently high, the resulting photoelectrode can exhibit PEC performance comparable to those obtainable from single-crystal or thin-film photoelectrodes.[22]

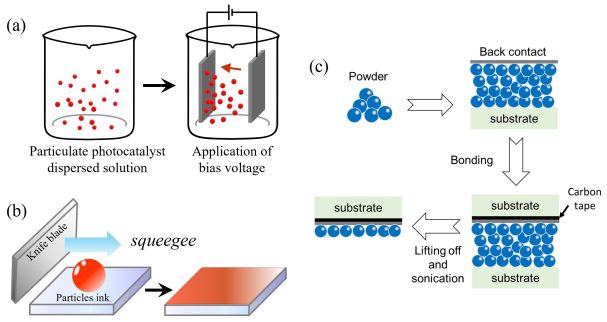

Figure 3. Diagrams showing typical fabrication processes for particulate photoelectrodes: (a) electrophoretic deposition, (b) doctor blading, and (c) particle transfer.

3. Design of Photocatalyst Materials

Since the first report of one-step OWS on a particulate $SrTiO_3$ photocatalyst,[6] many important photocatalyst materials capable of water splitting have been discovered. These compounds have included oxides, nitrides, oxynitrides, sulfides and oxysulfides. Figure 4 summarizes the band positions and bandgap energy levels for typical semiconductor photocatalyst materials used for water splitting. To allow one-step OWS, the band positions, meaning the CBM and VBM, should theoretically straddle the redox potential of water. One-step OWS using Ga_2O_3:Zn as the sole photocatalyst has been reported, with an external quantum efficiency (EQE) in excess of 70% under UV light (254 nm).[24] Other studies have established that an Al-

© 2024 The Authors. ChemSusChem published by Wiley-VCH GmbH

1864564x, 2024, 21, Downloaded from https://chemistry-europe.onlinelibrary.wiley.com/doi/10.1002/cssc.202400663 by Turkey Cochrane Evidence Aid, Wiley Online Library on [04/09/2026]. See the Terms and Conditions (https://onlinelibrary.wiley.com/terms-and-conditions) on Wiley Online Library for rules of use; OA articles are governed by the applicable Creative Commons License

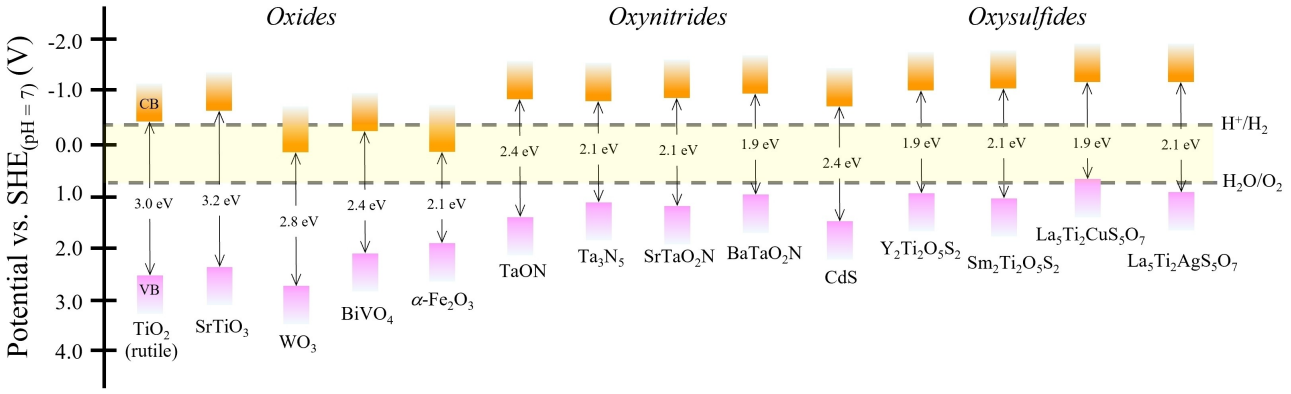

Figure 4. A band diagram summarizing the characteristics of photocatalyst materials (oxides, oxynitrides and oxysulfides) discussed herein. The energy levels are indicated as potentials vs. a standard hydrogen electrode (SHE) at a pH of 7. The standard redox potentials for the HER and OER at this pH are −0.41 V vs. SHE and 0.82 V vs. SHE, respectively. The orange and purple bars indicate the conduction band (CB) and valence band (VB), respectively.

doped $SrTiO_3$ (STO:Al) photocatalyst can provide an EQE as high as 56% in response to irradiation at a wavelength of 365 nm.[3b] More recent work has demonstrated that STO:Al coloaded with a Cr_2O_3/Rh cocatalyst for the HER and a CoOOH cocatalyst for the OER can promote one-step OWS with an EQE of almost 100%.[25] However, $SrTiO_3$ has a bandgap energy of 3.2 eV, which limits the maximum STH energy conversion efficiency to less than 1%.

Visible-light-responsive (oxy)nitrides and (oxy)sulfides, which can absorb visible light up to a 600 nm absorption edge (Figure 4), are promising photocatalyst materials that could potentially provide high STH efficiencies. A GaN:ZnO photocatalyst, comprising a solid solution of GaN and ZnO, has also been developed and has shown an EQE of 5.1% in response to irradiation at 410 nm.[26] Visible-light-responsive photocatalysts with absorption edge wavelengths in the vicinity of 600 nm that are suitable for water splitting have also been developed, including $LaMg_{1/3}Ta_{2/3}O_2N$ (a solid solution of $LaMg_{2/3}Ta_{1/3}O_3$ and $LaTaON_2$),[27] and nanorod-like Ta_3N_5 particles grown on $KTaO_3$.[28] Moreover, one-step OWS by $Y_2Ti_2O_5S_2$ particulate photocatalysts has been reported.[29] If these photocatalytic materials having absorption edges greater than 600 nm can be designed to provide one-step OWS with an EQE of at least 60%, STH efficiencies over 10% could be achieved.[30] Consequently, at present, research interest is shifting from the development of UV-responsive materials to studies of visible-light-responsive photocatalysts.

This section focuses on the recent development of OWS-compatible particulate photocatalysts based on oxides ($SrTiO_3$), oxynitrides ($BaTaO_2N$, $SrTaO_2N$) and oxysulfides ($Y_2Ti_2O_5S_2$). The effects of surface modification with cocatalysts on photocatalytic water splitting activity and the results of PEC analyses of interfacial properties using particulate photoelectrodes are also discussed in detail.

3.1. $SrTiO_3$ Photocatalysts

One-step OWS to produce hydrogen and oxygen in the expected stoichiometric ratio using NiO/$SrTiO_3$ as a particulate photocatalyst suspended in pure water was demonstrated in 1980.[6a] Since then, many attempts have been made to increase the efficiency of water splitting reactions using $SrTiO_3$ as the photocatalyst, including techniques such as facet engineering,[31] cation doping[32] and surface modifications with functional layers.[33] The challenge associated with using semiconductor photocatalysts to decompose water into hydrogen and oxygen is that the photochemical reaction is a reversible, multi-electron transfer process. During the interval between the completion of these multi-electron transfers and the extraction of the hydrogen and oxygen, competing electron transfer processes can occur in the reverse direction. The water splitting efficiency thus tends to be very low because the reverse electron transfer is actually preferred on a thermodynamic basis. Suppressing this reverse electron transfer while promoting forward electron transfer is the key to developing highly efficient photocatalysts. Readers interested in a systematic discussion of the various recombination and reverse reaction pathways in photocatalytic and photosynthetic processes are encouraged to refer to other publications, e.g. reference [7] summarized by Osterloh.

During photocatalytic water splitting, photogenerated charge carriers (that is, electrons and holes) work simultaneously in proximity to one another (with distances on the micro- or nanometer scale) within a single particle, such that the respective reducing and oxidizing potentials are lowered. Therefore, it is necessary to separate the excitons (that is, to achieve charge separation) within each individual photocatalyst particle. This can be achieved via the anisotropic transfer of photoexcited charges.[25] Each $SrTiO_3$:Al particle typically comprises a single crystal with several different crystal planes exposed (Figure 5a).[25] Interestingly, excited electrons and holes are selectively transferred to different crystalline planes, resulting in the selective deposition of Cr_2O_3/Rh on the (100) facet and CoOOH on the (110) facet. The results of electrostatic

© 2024 The Authors. ChemSusChem published by Wiley-VCH GmbH

1864564x, 2024, 21, Downloaded from https://chemistry-europe.onlinelibrary.wiley.com/doi/10.1002/cssc.202400663 by Turkey Cochrane Evidence Aid, Wiley Online Library on [04/09/2026]. See the Terms and Conditions (https://onlinelibrary.wiley.com/terms-and-conditions) on Wiley Online Library for rules of use; OA articles are governed by the applicable Creative Commons License

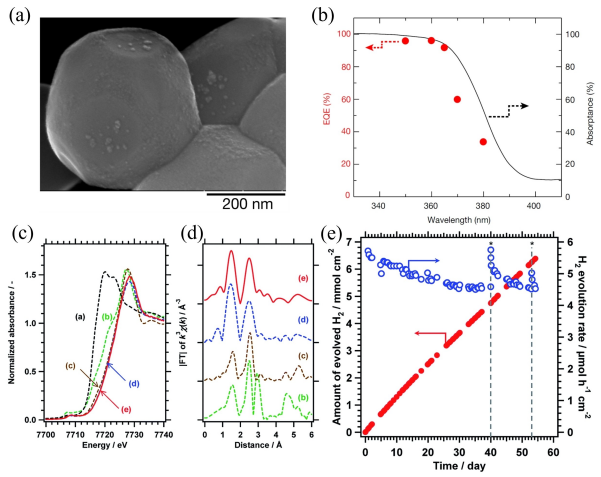

Figure 5. One-step OWS on an Al-doped $SrTiO_3$ particulate photocatalyst modified with a Cr_2O_3/Rh cocatalyst for the HER and a CoOOH cocatalyst for the OER. (a) An SEM image of the Cr_2O_3/Rh/$SrTiO_3$:Al/CoOOH photocatalyst. (b) The EQE during OWS as a function of wavelength. Reproduced from ref. [25] with permission. (c) Co–K edge XANES spectra and (d) Fourier transforms of k^3-weight Co–K EXAFS spectra. (e) The time-course of OWS on a TiO_2/CoOOH/$RhCrO_x$/$SrTiO_3$:Al photocatalyst sheet (5×5 cm^2) under simulated AM 1.5G solar illumination. The red and blue plots indicate the amount of evolved hydrogen and the rate of hydrogen evolution, respectively. Reproduced from ref. [33a] with permission from the Royal Society of Chemistry.

simulations suggested that $SrTiO_3$:Al particles have a work function difference of 0.2 eV between the (110) and (100) facets.[25] Recently, Assavachin et al. quantitatively evaluated the charge separation ability of the (100), (110), and (111) facets during PEC OER using hydrogen-annealed $SrTiO_{3-x}$ single crystals.[34] Comprehensive analyses, including (photo)electroanalytical measurements and surface photovoltage spectroscopy, indicate that the (110) facet of $SrTiO_{3-x}$ forms the strongest band bending with the O_2/H_2O redox couple at the solid/liquid interface, followed by the (111) and (100) facets.[34] This suggests that the (110) facet of $SrTiO_3$ is most suitable for hole accumulation, while the (100) facet is most suitable for electron accumulation. The measured work function difference between the (110) and (100) facets has been reported to be 0.16 eV,[34] which is in good agreement with the value calculated from electrostatic simulations. This work function difference likely induces anisotropic charge separation in $SrTiO_3$:Al particles.

Hence, cocatalysts can be selectively loaded on the surfaces of these particles to promote the HER and OER. When these cocatalysts are loaded by photo-deposition, photoexcited electrons move to the surface and reduce metal ions to deposit a metal whereas holes move to the surface and oxidize metal ions to deposit a metal oxide. Each material functions as a cocatalyst to promote the HER and OER (Figure 5a). If anisotropic charge transfer is used for photo-deposition, the HER and OER cocatalysts can be selectively deposited on different crystal facets of the $SrTiO_3$:Al.

Metals such as Rh are typically used as HER cocatalysts for particulate photocatalysts, with a surface coating of Cr_2O_3. In addition, CoOOH often serves as the OER cocatalyst. Compared with the conventional impregnation method in which the cocatalysts are randomly dispersed on the particulate photocatalyst surface, the OWS rate can be approximately doubled using this technique. An EQE close to 100% in the 350–360 nm range has also been reported (Figure 5b),[25] indicating that almost all the absorbed photons are used for the one-step OWS. This prior work represented the first-ever report of water splitting with a near-perfect quantum yield. The local structure and valence state of the Co species loaded on the $SrTiO_3$:Al were investigated by X-ray absorption fine structure (XAFS) analyses. As shown in Figures 5c and 5d, Co–K edge X-ray absorption near edge structure (XANES) data and the Fourier transformed k^3-weight extended XAFS (EXAFS) spectra revealed that the Co species were selectively dispersed on the photocatalyst surface as CoOOH using the photo-deposition method.[33a] The valence state and structure of the CoOOH on the $SrTiO_3$:Al (in which Co was in the Co^{3+} state) were found to be unchanged during a 15 h OWS trial (Figure 5d).[33a] The durability of a $SrTiO_3$:Al photocatalyst fixed on a 5×5 cm^2 glass plate was improved by surface modification with a protective TiO_2 layer. $SrTiO_3$:Al coated with TiO_2 and coloaded with $RhCrO_x$ and CoOOH as cocatalysts maintained its initial rate of gas evolution during a continuous 1000 h experiment under simulated AM 1.5G solar illumination (Figure 5e).[33a]

Because it is simple to apply immobilized photocatalyst particles to a substrate, it is expected that large-area photocatalyst panels will be easier to produce than photovoltaic solar panels. Figure 6a shows a photocatalyst sheet reactor with a light-receiving area (meaning a photocatalyst-coated area) of 625 cm^2.[3a] In this system, a water layer with a thickness of 100 μm is inserted between the $SrTiO_3$-based photocatalyst

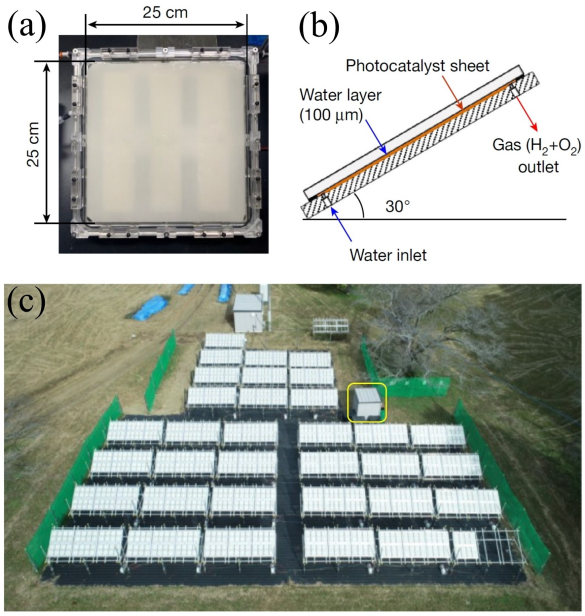

Figure 6. A 100 m^2 water splitting photocatalyst panel reactor. (a) A photograph of a panel reactor unit (625 cm^2). (b) The structure of the panel reactor unit viewed from the side. (c) An overhead view of the 100 m^2 solar hydrogen production system. The yellow box indicates a hut housing a gas separation facility. Reproduced from ref. [3a] with permission.

© 2024 The Authors. ChemSusChem published by Wiley-VCH GmbH

1864564x, 2024, 21, Downloaded from https://chemistry-europe.onlinelibrary.wiley.com/doi/10.1002/cssc.202400663 by Turkey Cochrane Evidence Aid, Wiley Online Library on [04/09/2026]. See the Terms and Conditions (https://onlinelibrary.wiley.com/terms-and-conditions) on Wiley Online Library for rules of use; OA articles are governed by the applicable Creative Commons License

sheet and a thin sheet of UV-transparent glass (Figure 6b). A mixture of gaseous hydrogen and oxygen is produced by the photocatalyst sheet in response to sunlight and is collected. By connecting 1600 of these photocatalyst sheet reactors side by side, a 100 m^2 scale photocatalyst plant for OWS was fabricated (Figure 6c). A long-term outdoor demonstration was conducted and this facility was found to operate in a safe, stable manner while producing large volumes of hydrogen and oxygen with continuous separation of these gases.

Figure 7 summarizes the structural and PEC characteristics of $SrTiO_3$:Al particulate photoelectrodes prepared through a particle transfer method (Figure 3c).[35] The SEM image in Figure 7a indicates the densely packed surface morphology of the $SrTiO_3$:Al particles. The cross-sectional SEM image (Figure 7b) and the energy dispersive X-ray spectroscopy (EDS) map that was simultaneously obtained (Figure 7c) demonstrate firm attachment of the $SrTiO_3$:Al particles, facilitated by the Ta/Ti back contact layer. Moreover, the Ta contact layer can be seen to be distributed between the electrode surfaces (Figure 7c), serving as an intermediary between the $SrTiO_3$:Al particles and the Ti conductor layer.

Figure 7d presents current-potential curves obtained from a $SrTiO_3$:Al particulate photoelectrode (denoted herein as STO/Ta(PT)) and a Nb-doped $SrTiO_3$ single-crystal wafer (denoted as STO/Ta(SC)).[35] The latter photoelectrode has an onset potential that is approximately 0.1 V more negative than that of the STO/Ta(PT). However, the photocurrent density generated by the STO/Ta(PT) at photoelectrode potentials more positive than 0.0 V_{RHE} was significantly higher than the value for the STO/Ta(SC). The incident photon-to-current conversion efficiency (IPCE) spectra of both the STO/Ta(PT) and STO/Ta(SC) recorded at an photoelectrode potential of 1.23 V_{RHE} are shown in Figure 7e.[35]

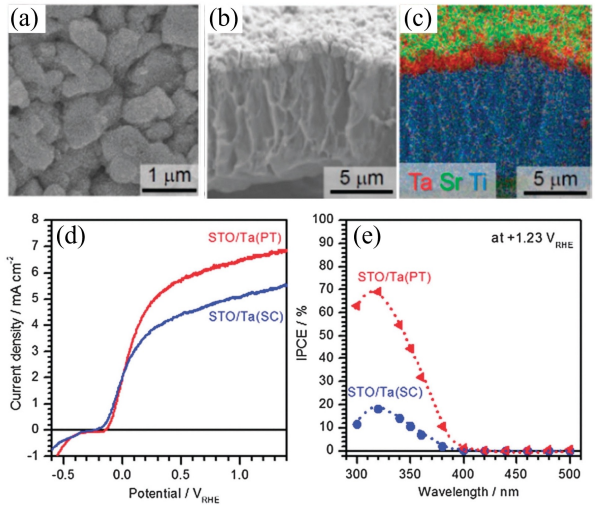

Figure 7. Structural and PEC properties of Al-doped $SrTiO_3$ particulate photoelectrodes (STO/Ta(PT)) prepared by a particle transfer method. (a) An overhead SEM image of the STO/Ta(PT). (b) A cross-sectional SEM image and (c) EDS map of an STO/Ta(P) particulate photoelectrode. (d) Photocurrent density-potential curves obtained from STO/Ta(PT) and a Nb-doped $SrTiO_3$ single crystal wafer (STO/Ta(SC)) in 0.1 M Na_2SO_4 with pH adjusted to 13 by the addition of NaOH, using a 300 W Xe lamp equipped with a cold mirror ($\lambda > 300$ nm). (d) IPCE spectra generated at 1.23 V_{RHE}. Reproduced from ref. [35] with permission from the Royal Society of Chemistry.

The STO/Ta(PT) demonstrated superior IPCE values compared with the STO/Ta(SC) at all wavelengths. The maximum IPCE exhibited by the STO/Ta(PT) was 69% at 320 nm. Photoelectrodes derived from photocatalyst particles have provided comparable performance to those fabricated from the corresponding single crystals. This prior work was the first demonstration of this phenomenon. Furthermore, such electrodes have the potential to provide even higher IPCE values because their structures are well suited to the absorption of light and the efficient utilization of photo-excited carriers.

$SrTiO_3$ photocatalysts are capable of performing one-step OWS, but their light absorption is limited to the UV region. To extend the light absorption of $SrTiO_3$ photocatalysts into the visible light region, extensive research has been conducted on cation doping at both Sr and Ti sites. This enhancement in optical absorption beyond 500 nm has been achieved by (co)doping with metals such as Sb, Rh, Cr, Mn, Ru, La, Ta, and Ir.[36] For instance, Ir doping can extend the absorption wavelength to 580 nm.[36b] However, a transition of Ir from Ir^{4+} to Ir^{3+} significantly reduces the activity.[32c] While increased visible light absorption by cation doping does not necessarily improve HER rates, the valence state of the metal dopant is critical for the efficiency of the photocatalytic water splitting. Codoping $SrTiO_3$ with Cr and Ta has been shown to increase the HER rate, which is attributed to the change in Cr valence state from Cr^{6+} to Cr^{3+}.[36c] Doping $SrTiO_3$ with Rh results in the Rh^{4+} valence state, while codoping with Sb partially converts Rh^{4+} to Rh^{3+}, thereby increasing the HER rate.[36d] In addition, codoping with La and Rh further improves the water splitting efficiency. When $SrTiO_3$ is doped alone with Rh, it predominantly forms the Rh^{4+} valence state. However, codoping with La shifts the Rh valence state from Rh^{4+} to Rh^{3+} due to charge compensation, as shown by XPS analysis.[36e,37] The HER activity of La- and Rh-codoped $SrTiO_3$ ($SrTiO_3$:La,Rh) varies significantly with the Rh/La ratio.[36e,37] The $SrTiO_3$:La,Rh particulate photocatalyst was employed in a Z-scheme OWS. A photocatalyst sheet comprising $SrTiO_3$:La,Rh for HER and $BiVO_4$ for OER achieved an STH energy conversion efficiency of 1.1% in Z-scheme OWS.[17b]

3.2. Surface Modification with Cocatalysts

$(Ga_{1-x}Zn_x)(N_{1-x}O_x)_2$ and $(Zn_{1+x}Ge)(N_2O_x)_3$ are both stable photocatalysts that can decompose water into hydrogen and oxygen under visible light.[38] Both GaN and ZnO have large band gaps and can only absorb UV light. However, following the formation of a solid solution (GaN:ZnO), these materials can absorb visible light up to 500 nm.[39] GaN:ZnO modified with RuO_2 as a cocatalyst has also been found to promote one-step OWS,[38d] representing the first example of OWS in response to visible light.

The Development of a cocatalyst for photocatalytic water splitting is essential for improving STH energy conversion efficiency. The cocatalyst aids in the extraction of excited carriers (electrons and holes) from the photocatalysts under light irradiation, and it reduces the overpotential required to drive the HER and OER. Metals and metal oxides, including Pt,

© 2024 The Authors. ChemSusChem published by Wiley-VCH GmbH

1864564x, 2024, 21, Downloaded from https://chemistry-europe.onlinelibrary.wiley.com/doi/10.1002/cssc.202400663 by Turkey Cochrane Evidence Aid, Wiley Online Library on [04/09/2026]. See the Terms and Conditions (https://onlinelibrary.wiley.com/terms-and-conditions) on Wiley Online Library for rules of use; OA articles are governed by the applicable Creative Commons License

Rh, Ru, MnO_x, CoO_x, and RuO_x, are widely used as cocatalysts to provide efficient catalytic sites at the solid/liquid interface during photocatalytic water splitting.[40] Although noble metal-based cocatalysts facilitate carrier transfer in HER, they can also lead to undesirable reverse reactions, such as O_2 reduction and H_2O formation from the evolved H_2 and O_2. Mixed metal oxides, such as $RhCrO_x$ and $RhZrO_x$, have been used as HER cocatalysts due to their high activity and ability to suppress these reverse reactions.[41] Metal sulfides and metal phosphates, including NiS, MoO_xS_y, $CoMoS_x$, and CoP_i, have also been investigated as cocatalysts for water splitting.[42] Investigations of cocatalysts are ongoing, with the aim of further improving photocatalytic OWS activity.

One of the most impressive cocatalyst systems for photocatalytic OWS comprises the Rh-core and Cr_2O_3-shell morphology.[43] OWS over a GaN:ZnO photocatalyst has been found to proceed in conjunction with the use of Rh/Cr_2O_3 having a core/shell type structure as the cocatalyst (Figure 8a).[43] Even so, the mechanism by which this core-shell type structure promotes OWS remains unexplained. Yoshida et al. elucidated the mechanism by which a core/shell Rh/Cr_2O_3 cocatalyst enhances the HER by using electrochemical and *in situ* spectroscopic measurements to study a Cr_2O_3-coated Rh plate model electrode.[44] A model electrode was fabricated by electrochemically depositing a 1.8-3.5 nm thick Cr_2O_3 layer on a Rh metal plate. The proton adsorption/desorption equilibrium and current density values associated with the HER process using Cr_2O_3-coated and bare Rh electrodes were compared. During these trials, an infrared absorption band at 2039 cm^{-1} attributed to Rh–H stretching was observed. The results of this prior study suggest that the Cr_2O_3 layer does not impede the proton reduction associated with the HER process and that the HER primarily occurs at the Cr_2O_3/Rh interface (Figure 8b).[44]

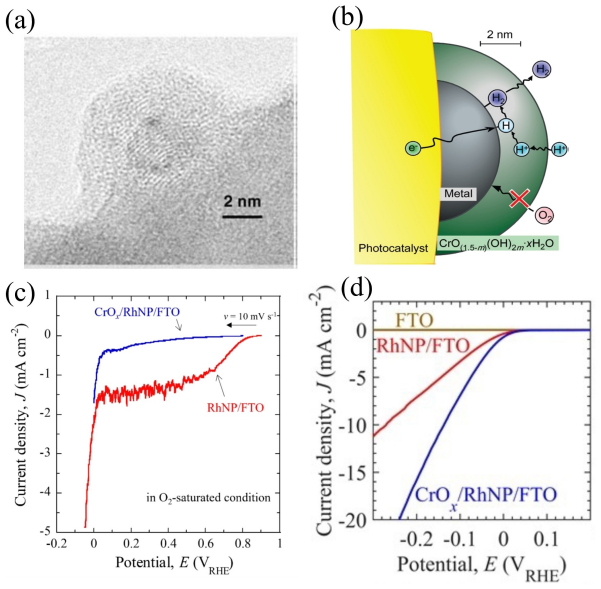

Figure 8. HER characteristics of a CrO_x-coated Rh (CrO_x/Rh) cocatalyst with a core/shell structure. (a) A high-resolution TEM image of the CrO_x/Rh cocatalyst loaded on a GaN:ZnO particulate photocatalyst (reproduced from ref. [43] with permission). (b) A model of selective HER on the core/shell (Rh/CrO_x) cocatalyst during photocatalytic OWS (adapted with permission from ref. [44]. Copyright 2009, American Chemical Society). (c) Current density-potential curves for CrO_x-coated Rh nanoparticles (CrO_x/RhNP) deposited on a conductive FTO substrate as obtained in a 0.5 M potassium phosphate buffered aqueous solution (pH = 7) under O_2-saturated conditions. (d) Linear sweep voltammograms acquired from CrO_x/RhNP/FTO, RhNP/FTO (without CrO_x) and bare FTO in 0.5 M KP_i (pH = 7) with a potential sweep rate of −10 mV s^{-1} under Ar. Reproduced from ref. [45] with permission.

The author's group recently demonstrated that Rh nanoparticles (Rh NPs) enveloped in an ultrathin layer of chromium oxide (CrO_x) can serve as a model electrode for the Cr_2O_3/Rh-metal core-shell-type cocatalyst system used in photocatalytic OWS.[45] An electrodeposition process was employed to apply a CrO_x layer onto Rh NPs previously coated onto a transparent conductive FTO substrate. The oxygen reduction reaction (ORR) was only inhibited in trials using the CrO_x/Rh NPs model electrode (Figure 8c). It appears that the CrO_x layer was permeable to protons and was able to generate hydrogen molecules while restricting the access of oxygen. The presence of the CrO_x layer on the Rh NPs also promoted electron transfer at the CrO_x/Rh NPs interface, thereby enhancing the current density during the HER (Figure 8d). Electrochemical AC Impedance spectroscopy demonstrated that the CrO_x layer facilitated proton transfer to the Rh NP surfaces via a H^+-hopping mechanism during the HER.[45]

The CrO_x also impeded electron transfer from the FTO to the electrolyte and/or Rh NPs while constraining the backward reaction by limiting oxygen migration. Porous layers made of metal oxides such as lanthanide oxides, SiO_x, MoO_x, ZrO_x or Al_2O_3 are reported to mitigate the reverse reaction during photocatalytic OWS.[46] Such work has highlighted the important role of an ultrathin CrO_x layer on nanoparticulate cocatalysts and provides cocatalyst design strategies that should help to achieve efficient photocatalytic OWS.

3.3. Nitride and Oxynitride Photocatalysts

Attempts to improve the performance of visible-light-responsive photocatalysts on metal oxides initially involved shifting the VBM to a more negative position while maintaining the position of the CBM. Such work allowed nitrides and oxynitrides to emerge as promising photocatalysts.[11] Due to the lower electronegativity of nitrogen compared with oxygen, the p-orbital associated with an N^{3-} anion creates a valence band on the negative side of the O 2p orbital. This results in a negative displacement of the VBM while preserving the CBM level of the metal oxide so as to narrow the bandgap (Figure 4). This adjustment improves the response of the material to visible light.

Often, the EQE associated with water splitting (the ratio of photons utilized in the target reaction to the total number of incident photons) tends to decrease with increasing response wavelength in water splitting reactions. This phenomenon arises from the reduced energy of the excited state attributable to narrower band gaps and challenges in synthesizing high-quality materials. Consequently, identifying improved techniques for the synthesis of photocatalytic materials that are responsive to visible light and finding innovative methods of

© 2024 The Authors. ChemSusChem published by Wiley-VCH GmbH

18645564x, 2024, 21, Downloaded from https://chemistry-europe.onlinelibrary.wiley.com/doi/10.1002/cssc.202400663 by Turkey Cochrane Evidence Aid, Wiley Online Library on [04/09/2026]. See the Terms and Conditions (https://onlinelibrary.wiley.com/terms-and-conditions) on Wiley Online Library for rules of use; OA articles are governed by the applicable Creative Commons License

activating these materials remain crucial research objectives. The lifetimes of excited states during OWS is short, leading to rapid recombination and the loss of electrons and holes on the sub-microsecond time scale or even faster (Figure 1).[2a] Moreover, the surfaces of the majority of semiconductors actually exhibit limited activity for redox reactions. Hence, it becomes imperative to employ cocatalysts to enhance water splitting (that is, to promote the HER and OER) and facilitate charge separation on the catalyst surface.

This section summarizes recent progress in the development of nitride- and oxynitride-based particulate photocatalysts. Ta_3N_5 is the primary nitride-based photocatalyst examined in detail. Oxynitrides such as $BaTaO_2N$, $SrTaO_2N$, $BaNbO_2N$, $SrNbO_2N$, $LaNbON_2$, and $LaTiO_2N$ have extensively been reported as visible-light-responsive particulate photocatalysts for water splitting. This section specifically focuses on Ta_3N_5, $BaTaO_2N$, and $SrTaO_2N$, which have shown significant progress in recent years and have been demonstrated by the author's group to be capable of one-step OWS. Recent advances in particulate photocatalysts containing Nb and Ti ($BaNbO_2N$,[47] $SrNbO_2N$,[48] $LaNbON_2$,[49] and $LaTiO_2N$[50]) are referred to in other publications. This section also demonstrates the effects of synthetic procedures, specifically the nitridation reaction conditions (meaning duration and temperature) and of surface modifications with cocatalysts. The intrinsic semiconductor characteristics of these materials when made into photoelectrodes as determined using electroanalytical techniques are also assessed.

3.3.1. Tantalum Nitride Photocatalysts

In early 2000s, it was reported that tantalum nitride (Ta_3N_5) possesses a band structure capable of absorbing visible light within the wavelength range of 400 to 600 nm, thus facilitating the decomposition of water into hydrogen and oxygen.[51] Nevertheless, the utilization of Ta_3N_5 particulate photocatalysts for water splitting remained unrealized because the conventional synthesis method involved prolonged heating of the oxide precursor in a flow of gaseous ammonia, resulting in challenges in synthesizing high-quality nitride photocatalysts. Consequently, there have been studies focused on finding alternative starting materials and synthesis conditions.

The nitridation reactions of oxides such as potassium tantalate oxide ($KTaO_3$) can be accomplished in less than 1/10th of the time required by conventional methods (using Ta_2O_5 as a starting material).[28] In prior work, single-crystal Ta_3N_5 nanorods were directly formed on edges of $KTaO_3$ particles. These nanorods comprised distinct single crystals with each rod spatially separated and without grain boundaries (Figure 9a). Single-crystal Ta_3N_5 nanorods grown on $KTaO_3$ ($Ta_3N_5/KTaO_3$) were also loaded with a Rh/Cr_2O_3 core/shell cocatalyst via photo-deposition (Figure 9b). The resulting surface-modified Ta_3N_5 nanorods were found to promote one-step OWS to produce hydrogen and oxygen under simulated AM 1.5G solar illumination (Figure 9c).[28] This research confirmed the importance of using nanostructured single-crystal photocatalysts without structural defects in sunlight-driven water splitting.

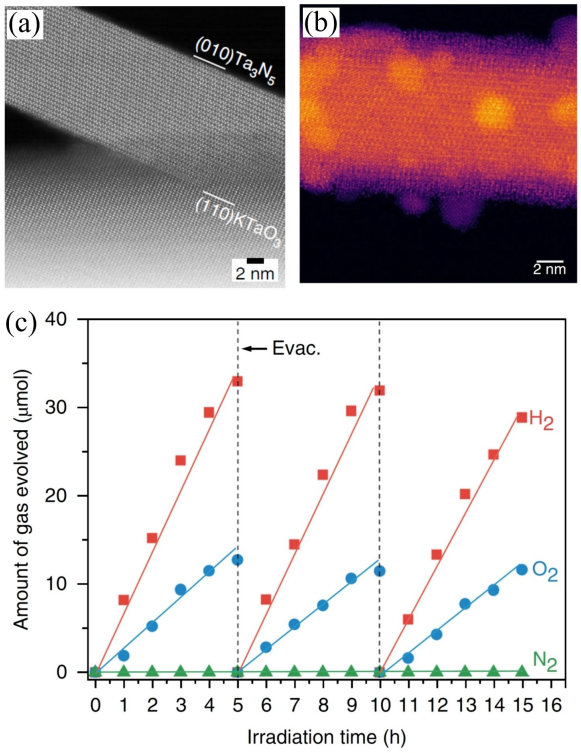

Figure 9. One-step OWS on Ta_3N_5 nanorods grown on $KTaO_3$ ($Ta_3N_5/KTaO_3$) as a particulate photocatalyst. (a) An annular-dark field scanning transmission electron microscopy (ADF-STEM) image of the $Ta_3N_5/KTaO_3$. The lines indicate the (010) and (110) crystal facets of the Ta_3N_5 and $KTaO_3$, respectively. (b) An ADF-STEM image of a Rh cocatalyst deposited on the Ta_3N_5 nanorods. (c) Gas evolution over time during OWS over a Cr_2O_3/Rh-modified $Ta_3N_5/KTaO_3$ particulate photocatalyst under simulated AM 1.5G solar illumination. The dashed lines indicate the points at which illumination was restarted after the removal of gas products by evacuation (indicated as "Evac."). Reproduced from ref. [28] with permission.

Ta_3N_5 is one of the most promising photocatalytic materials for water splitting but it remains difficult to drive OWS solely using Ta_3N_5 in conjunction with one-step photoexcitation (with the exception of $Ta_3N_5/KTaO_3$). However, Ta_3N_5 photocatalysts have been employed to promote Z-scheme type OWS.[37,52] In particular, Z-scheme water splitting systems based on Ta_3N_5 and electron mediators (Figure 2b), photocatalyst sheets prepared by the particle transfer method (Figure 2c) and solid/solid heterostructures have been established.

Li's group developed a $Ta_3N_5/BaTaO_2N$ (BTON) composite having a $Ta_3N_5/BaTaON_2$ heterostructure and used this material to create a particle-to-particle Z-scheme OWS system responsive to visible light.[53] As shown in Figure 10a, these particles had a homogeneous morphology. The Ta_3N_5 and $BaTO_2N$ phases were difficult to distinguish simply by SEM observations, demonstrating the formation of a true nanocomposite. The accompanying EDS map establishes that Ta originating from both the Ta_3N_5 and $BaTaO_2N$ was widely dispersed while Ba derived from the $BaTaO_2N$ was present in specific locations on the Ta_3N_5 (Figure 10b).

© 2024 The Authors. ChemSusChem published by Wiley-VCH GmbH

1864564x, 2024, 21, Downloaded from https://chemistry-europe.onlinelibrary.wiley.com/doi/10.1002/cssc.202400663 by Turkey Cochrane Evidence Aid, Wiley Online Library on [04/09/2026]. See the Terms and Conditions (https://onlinelibrary.wiley.com/terms-and-conditions) on Wiley Online Library for rules of use; OA articles are governed by the applicable Creative Commons License

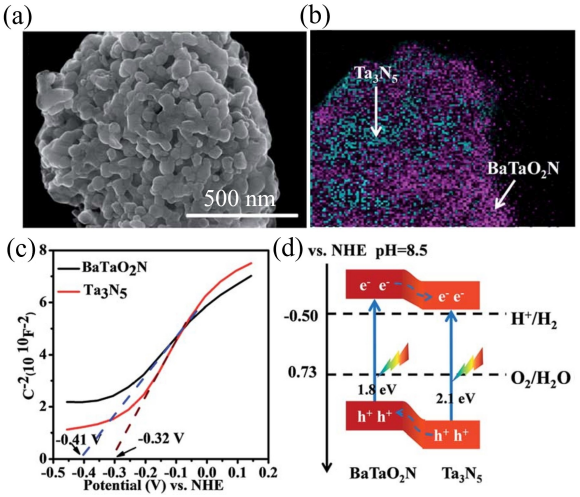

Figure 10. OWS on a Ta_3N_5/$BaTaO_2N$ composite particulate photocatalyst under visible light. (a) An SEM image and (b) EDS map of the photocatalyst (scale bar: 500 nm). (c) Mott-Schottky (MS) plots obtained from Ta_3N_5 and $BaTaO_2N$ particulate photoelectrodes prepared using an electrophoretic deposition method. The electrolyte and alternating current frequency were 0.5 M Na_2SO_4 with pH adjusted to 8.5 by the addition of NaOH and 1000 Hz, respectively. The intercept of the dashed lines against the photoelectrode potential (*x*-axis) indicates the location of the flatband potential. (d) A schematic depiction of the band structure of the Ta_3N_5/$BaTaO_2N$ heterostructure based on the MS analysis of the particulate photoelectrode. Reproduced from ref. [53] with permission from the Royal Society of Chemistry.

The semiconducting characteristics of the electrified solid/liquid interface of Ta_3N_5 and $BaTaO_2N$ particulate photoelectrodes fabricated through an electrophoretic deposition method were evaluated using an Mott-Schottky (MS) analysis (Figure 10c).[53] The flatband potentials of Ta_3N_5 and $BaTaO_2N$ were calculated to be approximately 0.32 and 0.41 V vs. a normal hydrogen electrode (NHE), respectively (Figure 10c). Based on the difference in the flatband potentials of these two compounds, an energy level diagram for the Ta_3N_5/$BaTaO_2N$ heterostructure was constructed as depicted in Figure 10d. This heterostructure facilitated the migration of photogenerated electrons from the CB of $BaTaO_2N$ to that of Ta_3N_5. Simultaneously, photogenerated holes in the VB were transferred in the opposite direction (that is, to the $BaTaO_2N$), leading to spatial charge separation.[53] This system can be regarded as a good example of an OWS process that successfully utilizes the spatial distribution of charge carriers due to a difference in electron energy positions between nitride and oxynitride photocatalyst particles.

3.3.2. Barium Tantalum Oxynitride Photocatalysts

Tuning the morphology of $BaTaO_2N$ to improve its OWS activity has been a challenging goal that has been pursued for the past several decades. Various methods for the preparation of $BaTaO_2N$ particulate photocatalysts have been examined, including the utilization of a salt-based flux,[54] cation doping[55] and surface modification with cocatalysts.[56] The resulting $BaTaO_2N$ particles have been shown to promote half-reactions evolving either hydrogen or oxygen in the presence of sacrificial reagents (methanol for the HER and $AgNO_3$ for the OER) when used in two-step Z-scheme OWS.[55e,56b,57] Despite this, the application of this compound to one-step OWS remains challenging. In 2022, the author's group reported the first demonstration of one-step OWS using a Mg-doped $BaTaO_2N$ particulate photocatalyst loaded with Cr_2O_3/Na–Rh and IrO_2 as cocatalysts.[58] Interestingly, minimal activity was observed without Mg doping, indicating that the performance of the $BaTaO_2N$ originated from doping.

In 2023, the author's group achieved one-step OWS using a non-doped $BaTaO_2N$ particulate photocatalyst. The $BaTaO_2N$ employed in this work was prepared by the nitridation of a mixture of amorphous Ta_2O_5 and $BaCO_3$.[59] The non-doped $BaTaO_2N$ surface was modified with a Cr_2O_3/Rh core-shell HER cocatalyst and an IrO_2 OER cocatalyst (Figures 11a–d). The resulting Cr_2O_3/Rh/$BaTaO_2N$/IrO_2 photocatalyst showed stoichiometric hydrogen and oxygen evolution under visible light illumination (Figure 11e). Importantly, this material did not undergo self-photooxidation to form oxides with the concurrent generation of nitrogen gas. An apparent quantum yield (AQY) of 0.107% was obtained in response to 400 nm light.[59] The OWS activity of this $BaTaO_2N$ photocatalyst was greatly affected by the nitridation conditions, including the duration and temperature (Figure 11f). Specifically, a prolonged nitridation time produced single phase $BaTaO_2N$ showing significantly lower water splitting activity.

Determining the nitridation factors affecting the water splitting activity of the $BaTaO_2N$ particles is crucially important to the development of more efficient particulate photocatalysts based on oxynitride materials. The electrochemical properties of $BaTaO_2N$ with water splitting activity (Active-BTON) and without activity (Inactive-BTON) were evaluated using particulate photoelectrodes prepared through a particle transfer method (Figure 3c).

Figure 12a shows MS plots obtained from the Active- and Inactive-BTON particulate photoelectrodes in aqueous 1 M potassium phosphate solutions having various pH values.[60] The Active-BTON demonstrated a higher $1/C^2$ value (the reciprocal of the surface capacitance) compared with the Inactive-BTON across the measured direct current potential range. Notably, the $1/C^2$ values for the Active-BTON were approximately 8–10 times greater than those for the Inactive-BTON. This disparity suggests that the carrier concentration associated with impurities and/or defects within the BTON was lower in the Active-BTON than in the Inactive-BTON. This finding agrees with the results of previous transient absorption spectroscopic (TAS) analyses, which indicated that photoexcited free electrons had a prolonged lifetime in Active-BTON particles compared with the Inactive-BTON.[59–60] The presence of long-lived free electrons, attributed to a reduced number of defects within the Active-BTON particles, is evidently vital to achieving one-step OWS. As shown in Figure 12b, both the Active- and Inactive-BTON photoelectrodes exhibited flatband potentials (E_{FB}) that were more negative than the standard HER redox potential (represented by the solid red line). The E_{FB} values were found to vary

© 2024 The Authors. ChemSusChem published by Wiley-VCH GmbH

1864564x, 2024, 21, Downloaded from https://chemistry-europe.onlinelibrary.wiley.com/doi/10.1002/cssc.202400663 by Turkey Cochrane Evidence Aid, Wiley Online Library on [04/09/2026]. See the Terms and Conditions (https://onlinelibrary.wiley.com/terms-and-conditions) on Wiley Online Library for rules of use; OA articles are governed by the applicable Creative Commons License

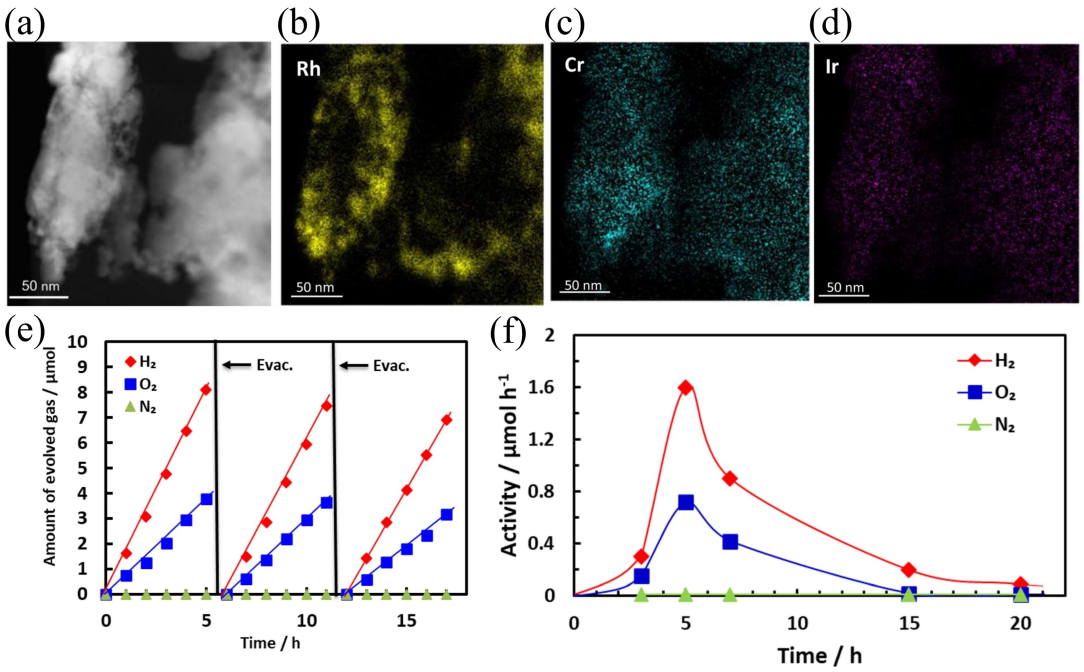

Figure 11. One-step OWS on a $BaTaO_2N$ particulate photocatalyst modified with Cr_2O_3/Rh as an HER cocatalyst and IrO_2 as an OER cocatalyst. (a–d) An ADF-STEM image and STEM-EDS maps of the Cr_2O_3/Rh/$BaTaO_2N$/IrO_2 photocatalyst. (e) The time course of gas evolution over Cr_2O_3/Rh/$BaTaO_2N$/IrO_2 under visible light (using a 300 W Xe lamp equipped with an L42 cut-off filter, $\lambda > 420$ nm). The solid vertical lines indicate the points at which illumination was restarted after the removal of gas products by evacuation (indicated as "Evac."). (f) The effect of nitridation time on the OWS activity over Cr_2O_3/Rh/$BaTaO_2N$/IrO_2. Reproduced from ref. [59] with permission from the Royal Society of Chemistry.

with the pH of the electrolyte, with a slope of 0.059 V. These data indicate that H^+ adsorption reached a state of equilibrium associated with the formation of hydroxy groups at the BTON/water interface.

The Active-BTON particulate photoelectrode provided higher IPCE values at 1.2 V_{RHE} compared with the Inactive-BTON (Figure 12c). The IPCE values for the former material were approximately twice those for the latter over the range of wavelengths assessed. The onset potentials and photocurrent densities for BTON-based particulate photoelectrodes were shown to be dependent on the electrocatalytic activity of the CoO_x-based cocatalyst. The OER activity of this cocatalyst was evaluated by liner sweep voltammetry and the data showed a shift in the OER onset potential with increasing pH of the electrolyte (Figure 12d).[60] Irrespective of the electrolyte pH, the photocurrent density generated by the Active-BTON photoelectrodes was twice that obtained from the Inactive-BTON photoelectrodes. The enhanced photocurrents and IPCE values associated with the Active-BTON are attributed to the improved semiconductor characteristics of this material, such as a lower carrier concentration (N_d). In future, it would be helpful to enhance the electrocatalytic activity of the cocatalyst loaded onto the photocatalyst as a means of increasing the water splitting efficiency of the BTON.

3.3.3. Strontium Tantalum Oxynitride Photocatalysts

Tantalum oxynitride perovskites, typically denoted as $ATaO_2N$ (where *A* represents Ca, Sr or Ba), are semiconducting materials that are more rarely used but that exhibit remarkable stability in aqueous environments. These compounds also show narrow E_g values ranging from 1.9 to 2.4 eV and appropriately situated conduction and valence bands capable of spanning the water redox potential.[57b] The previous section described recent progress in the development of $BaTaO_2N$ photocatalysts (where $A = Ba$) and the photocatalytic and PEC water splitting properties of these materials. Among the various possible $ATaO_2N$ compounds, $SrTaO_2N$ ($A = Sr$) has recently attracted attention due to the unique physical and chemical properties of this material, such as the band structure, photophysical characteristics and ferroelectric properties.[61] The absorption edge wavelength for $SrTaO_2N$ is at approximately 590 nm, corresponding to an E_g of 2.1 eV. Although this value is slightly larger than that for $BaTaO_2N$ ($E_g = 1.9$ eV), efficient water splitting can be realized if the defect concentration in the catalyst is reduced by increasing the degree of crystallinity. This section summarizes recent progress in the development of $SrTaO_2N$ particulate photocatalysts for water splitting.

To date, several methods of preparing $SrTaO_2N$ have been examined with the aim of improving the water splitting activity.[62] Reduced Ta ions (Ta^{3+} and/or Ta^{4+}) in this material are thought to act as carrier recombination centers.[57b,62b] Consequently, the preparation of solid solutions or single crystals of $SrTaO_2N$ has been extensively investigated as a

© 2024 The Authors. ChemSusChem published by Wiley-VCH GmbH

1864564x, 2024, 21, Downloaded from https://chemistry-europe.onlinelibrary.wiley.com/doi/10.1002/cssc.202400663 by Turkey Cochrane Evidence Aid, Wiley Online Library on [04/09/2026]. See the Terms and Conditions (https://onlinelibrary.wiley.com/terms-and-conditions) on Wiley Online Library for rules of use; OA articles are governed by the applicable Creative Commons License

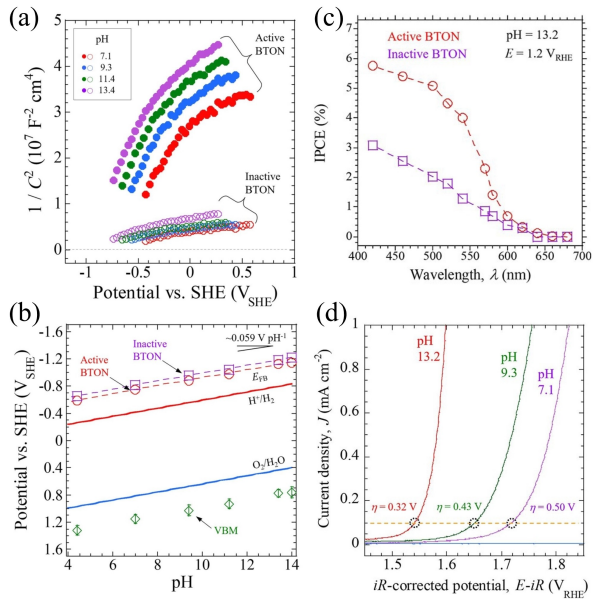

Figure 12. The PEC performance of $BaTaO_2N$ particulate photoelectrodes prepared through a particle transfer method using $BaTaO_2N$ exhibiting OWS activity (Active-BTON) and not exhibiting OWS activity (Inactive-BTON). (a) MS plots obtained from Active- and Inactive-BTON particulate photoelectrodes as acquired in 1.0 M potassium phosphate aqueous solutions with pH values of 7.1, 9.3, 11.4 or 13.4. The AC potential modulation and AC frequency during these trials were 5 mV_{rms} and 1000 Hz, respectively. (b) The effect of pH on the flatband potential (E_{FB}) and valence band maximum (VBM) as estimated from the results of the MS analyses. (c) IPCE spectra obtained from Active- and Inactive-BTON photoelectrodes at a photoelectrode potential of 1.2 V_{RHE} and a pH of 13.2. (d) *iR*-corrected linear sweep voltammograms of a CoO_x cocatalyst deposited on a conductive FTO substrate immersed in 1.0 M potassium phosphate aqueous solutions with pH values of 7.1, 9.3 or 13.2 with a potential sweep rate of 10 mV s^{-1} under Ar. The overpotential (η) corresponds to the difference between the standard redox potential of the OER (1.23 V_{RHE}) and the electrode potential required to generate 0.1 mA cm^{-2}. Reproduced from ref. [60] with permission.

means of avoiding the generation of reduced Ta ions and related defects. Another promising strategy for improving water splitting activity is cation doping of $SrTaO_2N$. Various studies have assessed the effect of doping this compound with metal cations such as Sc^{3+}, Ga^{3+}, In^{3+} and Ce^{4+}, followed by nitridation to produce cation doped $SrTaO_2N$.[62b] In particular, the addition of Ga^{3+} has been found to significantly improve photocatalytic activity,[62b] although this material has not demonstrated one-step OWS.

In 2023, the first report of one-step OWS using a non-doped single-crystal $SrTaO_2N$ particulate photocatalyst with visible light was published.[63] This system required the preparation of a single-crystal specimen having a low defect concentration together with surface modification with an efficient cocatalyst. A single-crystal $SrTaO_2N$ particulate photocatalyst was prepared via the nitridation reaction of $SrCl_2$ and Ta_2O_5 together with NaOH, combined at a suitable molar ratio (meaning a NaOH/Ta_2O_5 molar ratio of 1). The $SrCl_2$ served as the Sr source as well as the flux salt and the NaOH functioned as both the O source and flux.

The OWS activity of this material was found to be affected by cocatalyst loading parameters, in particular the proportions of Ir, Ru and Cr contents in the cocatalyst.[63] The high-resolution X-ray photoelectron spectroscopy (HR-XPS) Ir 4f spectra (Figure 13A) obtained from IrO_x/Ru-coloaded $SrTaO_2N$ indicate that the peaks are shifted to lower binding energies, meaning that the IrO_x deposited by a microwave (MW) process affected the electronic structure of the Ru cocatalyst to produce Ru–Ir bimetallic oxides (denoted as $RuIrO_x$). The transient decay profiles for photogenerated electrons in the $RuIrO_x$-modified $SrTaO_2N$ decayed more rapidly than those in bare $SrTaO_2N$ and Ru-modified $SrTaO_2N$ particles, confirming the ability of the $RuIrO_x$ cocatalyst to capture electrons (Figure 13B). In addition, CrO_x-coated $RuIrO_x$ (CrO_x/$RuIrO_x$) was found to provide catalytic sites for the HER (Figure 13C) while suppressing the backward reaction ($H_2 + {}^1/_2O_2 \rightarrow H_2O$) and ORR. In contrast, RuO_x was able to capture photogenerated holes and so provided catalytic sites for the ORR (Figure 13C). The IrO_x species present at low concentrations may also have acted as recombination centers for carriers to reduce the OWS efficiency. Even so, it is likely that more efficient photocatalytic water splitting will be possible through more precise optimization of the cocatalyst loading method and the development of techniques for the facet-selective deposition of cocatalysts.

A remaining issue related to the use of Ta-based oxynitride photocatalysts is the requirement to reduce the density of

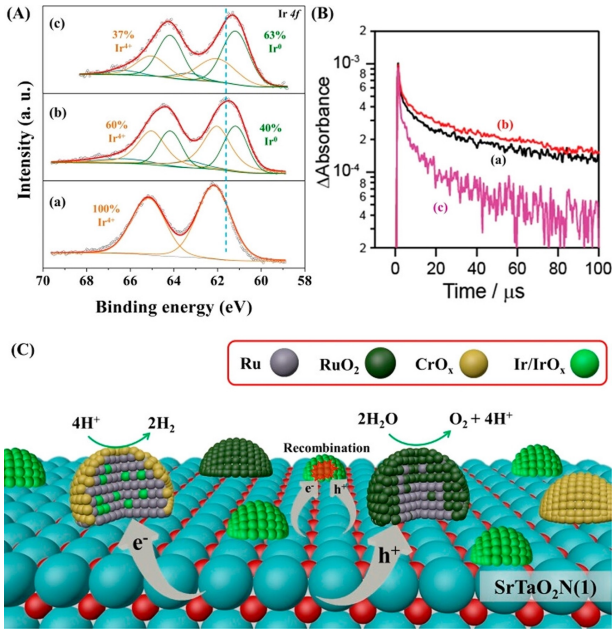

Figure 13. The interfacial design of a $SrTaO_2N$ particulate photocatalyst capable of one-step OWS under visible light. (A) HR-XPS Ir 4f spectra of $SrTaO_2N$ loaded with (a) IrO_2(MW), (b) IrO_2(MW) and reduced without loading Ru, and (c) Ru/IrO_2(MW). The MW means the cocatalyst modification under microwave treatment. (B) Transient decay profiles of photogenerated electrons in $SrTaO_2N$ probed at 5000 nm (a) without cocatalysts, (b) with loaded Ru, and (c) with loaded Ru/IrO_2(MW). (C) A diagram showing the carrier transfer process at the photocatalyst/cocatalyst/water interface. In this process, CrO_x-coated $RuIrO_x$, RuO_2 and IrO_x act as catalytic sites for the HER, OER and charge recombination, respectively. Adapted with permission from ref. [63]. Copyright 2023, American Chemical Society.

© 2024 The Authors. ChemSusChem published by Wiley-VCH GmbH

1864564x, 2024, 21, Downloaded from https://chemistry-europe.onlinelibrary.wiley.com/doi/10.1002/cssc.202400663 by Turkey Cochrane Evidence Aid, Wiley Online Library on [04/09/2026]. See the Terms and Conditions (https://onlinelibrary.wiley.com/terms-and-conditions) on Wiley Online Library for rules of use; OA articles are governed by the applicable Creative Commons License

carrier recombination centers (which are related to defects) that prevent efficient water splitting. The nitridation of precursor compounds in the presence of a flux has been investigated as one means of improving the crystallinity of oxynitrides. The precursor is typically the corresponding oxide (e.g. Ta_2O_5). Recently, a new synthetic route has been explored that uses tantalum sulfide (TaS_2, containing Ta^{4+}) as the starting material.[64] This process employs a mixture of TaS_2, a metal hydroxide ($A(OH)_2$, A = Ca, Sr or Ba) and a molten salt (e.g. $SrCl_2$) to produce highly crystalline Ta-based oxynitrides, specifically $SrTaO_2N$. These materials can have sub-50 nm particles with an absorption edge of 592 nm (Figures 14a and 14b).

The $SrTaO_2N$ prepared through this synthesis route had particles less than 50 nm in size and exhibited greatly improved promotion of the HER half-reaction in conjunction with a sacrificial reagent under visible light (Figure 14c).[64] These small, highly crystalline particles provided minimal distances for the migration of photoexcited charge carriers to active surface sites. This feature enabled the efficient injection of carriers into the cocatalyst and so reduced charge recombination at the particle/cocatalyst interface. An AQY of 3% at 420 nm for the HER half-reaction in the presence of sacrificial reagents was achieved (Figure 14d). This efficiency was two orders of magnitude greater than values previously reported for a $SrTaO_2N$ photocatalyst prepared by conventional nitridation using oxide precursors.[62b] However, these sub-50 nm $SrTaO_2N$ particles have not yet demonstrated one-step OWS. In future, it will be necessary to examine the factors limiting the activity of this material by analyzing the solid/liquid interfaces of particulate photoelectrodes. Nevertheless, the proposed synthetic strategy is expected to be applicable to a broad range of oxynitrides and optimized surface and cocatalyst modifications should enable efficient one-step OWS with high STH efficiency.

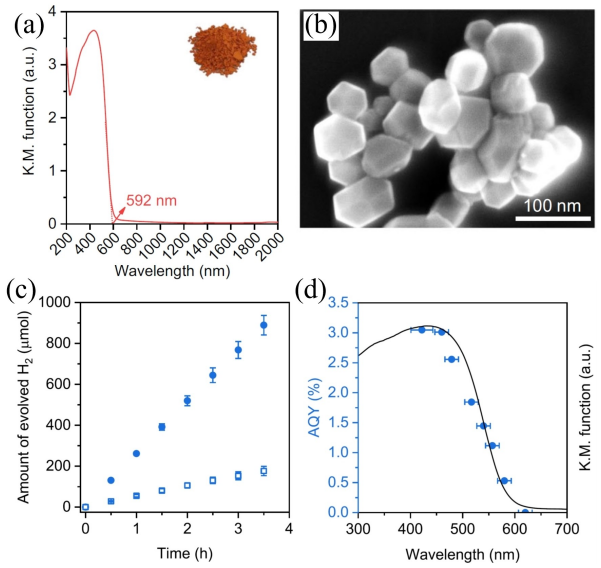

Figure 14. A sub-50 nm $SrTaO_2N$ particulate photocatalyst for visible-light-driven water splitting. (a) The UV-visible diffuse reflectance spectrum of sub-50 nm $SrTaO_2N$ nanocrystals. The inset shows the nanocrystals. (b) An SEM image of the $SrTaO_2N$ nanocrystals. (c) The time course of hydrogen evolution in an aqueous methanol (13 vol%) solution over the Cr_2O_3/Pt/$SrTaO_2N$/Ir nanocrystals (circles) derived from TaS_2 and large sized $SrTaO_2N$ particles (squares) derived from Ta_2O_5 under illumination from a 300 W Xe lamp with an L42 cut-off filter ($\lambda > 420$ nm). (d) A plot of apparent quantum yield (AQY) versus wavelength during the HER on $SrTaO_2N$ nanocrystals. The solid line indicates the UV-visible diffuse reflectance spectrum of the $SrTaO_2N$. Reproduced from ref. [64] with permission.

3.4. Oxysulfide Photocatalysts

Sulfide-based photocatalysts have demonstrated remarkable HER activity in response to visible light.[65] As an example, CdS nanorods and solid solutions are able to generate gaseous H_2 with a quantum efficiency of nearly 100% when a sacrificial reagent is present.[65b] Nevertheless, sulfide photocatalysts do not catalyze the OER because of the photooxidation of sulfide ions (S^{2-}). Consequently, achieving stable and efficient OWS with sulfide-based photocatalysts appears unlikely. Conversely, oxysulfides exhibit favorable photo-stability in aqueous environments under visible light. Oxysulfides are also expected to be more resistant to self-oxidation because surface S^{2-} ions are stabilized through the hybridization of S 3p and O 2p orbitals.[66] Compounds such as $Ln_2Ti_2O_5S_2$ (Ln = Y, Pr, Nd, Sm, Gd, Tb, Dy, Ho or Er) have demonstrated the capability to evolve H_2 and/or O_2 while displaying resistance to photocorrosion.[66] Specifically, $Y_2Ti_2O_5S_2$ (Ln = Y) loaded with cocatalysts has exhibited efficacy in promoting OWS.[29] There has been active research into the synthesis, modification and charge carrier dynamics of $Y_2Ti_2O_5S_2$ to evaluate its potential practical applications in solar-driven water splitting systems.[67]

In addition to $Ln_2Ti_2O_5S_2$-based photocatalysts, $La_5Ti_2MS_5O_7$ (M = Cu or Ag) compounds have been reported to function as visible-light-responsive oxysulfide photocatalysts.[68] A solid solution of $La_5Ti_2CuS_5O_7$ and $La_5Ti_2AgS_5O_7$ ($La_5Ti_2Cu_{0.9}Ag_{0.1}S_5O_7$, LTCA) has also shown an absorption edge wavelength of 710 nm, corresponding to a bandgap energy of 1.8 eV.[69] This LTCA photocatalyst was employed to produce particulate photoelectrodes to evaluate the applicability of this material to PEC cells promoting non-biased OWS (Figure 2d).

This section first examines the development of $Y_2Ti_2O_5S_2$ particulate photocatalysts and assesses the PEC properties of this material at the solid-liquid interface. The characteristics of LTCA-based photocatalysts and the associated PEC water splitting performance are also presented.

3.4.1. $Y_2Ti_2O_5S_2$ Photocatalysts

Among the $Ln_2Ti_2O_5S_2$ series of materials, $Y_2Ti_2O_5S_2$ (YTOS) particulate photocatalysts modified with cocatalysts were the first to exhibit one-step OWS under visible light without the addition of sacrificial reagents.[29] An E_g value for YTOS of approximately 1.9 eV was estimated on the basis of UV-visible diffuse reflectance spectroscopy (Figure 15a). Thus, a large portion of the solar spectrum can be utilized by this material.

In 2019, a YTOS particulate photocatalyst loaded with a core/shell type Cr_2O_3/Rh HER cocatalyst and IrO_2 OER cocatalyst showed stoichiometric hydrogen and oxygen production via

© 2024 The Authors. ChemSusChem published by Wiley-VCH GmbH

18645564x, 2024, 21, Downloaded from https://chemistry-europe.onlinelibrary.wiley.com/doi/10.1002/cssc.202400663 by Turkey Cochrane Evidence Aid, Wiley Online Library on [04/09/2026]. See the Terms and Conditions (https://onlinelibrary.wiley.com/terms-and-conditions) on Wiley Online Library for rules of use; OA articles are governed by the applicable Creative Commons License

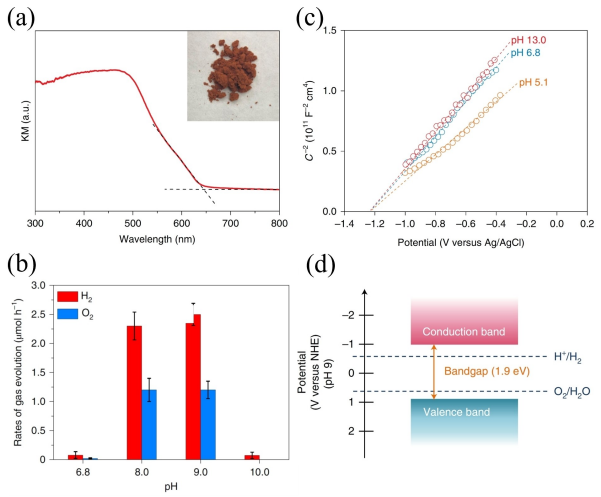

Figure 15. One-step OWS on a $Y_2Ti_2O_5S_2$ particulate photocatalyst. (a) UV-visible diffuse reflectance spectrum of the material. The inset shows a photographic image of the sample. (b) Gas evolution rates on Cr_2O_3/Rh/$Y_2Ti_2O_5S_2$/IrO_2 as functions of the pH of the reaction solution with irradiation by a 300 W Xe lamp equipped with a cutoff filter ($\lambda > 420$ nm). (c) MS plots of $Y_2Ti_2O_5S_2$ particulate photoelectrodes prepared by the particle transfer method acquired in 0.1 M Na_2SO_4 aqueous solutions with pH adjusted to 5.1, 6.8 or 13.0 by addition of H_2SO_4 or NaOH. The AC potential modulation and AC potential frequency were 10 mV_{rms} and 1000 Hz, respectively. (d) A band structure diagram for $Y_2Ti_2O_5S_2$. The energy levels here are relative to a normal hydrogen electrode at a pH of 9. Reproduced from ref. [29] with permission.

one-step OWS.[29] Since both sulfide and oxysulfide materials contain S^{2-} anions, it is important to inhibit photocorrosion (or self-photooxidation reactions) by applying an appropriate surface coating. Thermogravimetric analysis has shown that YTOS remains stable up to 700 °C in both air and N_2. Interestingly, this compound does not exhibit the considerable mass loss at approximately 600 °C that is typical of oxysulfides due to evaporation of sulfur. Furthermore, YTOS was found to resist self-photooxidation (which is normally a concern with sulfides) while evolving hydrogen and oxygen in stoichiometric amounts over a 24 h period.

The OWS activity of YTOS loaded with Cr_2O_3/Rh and IrO_2 is limited by the pH of the reaction solvent. As shown in Figure 15b, YTOS provided stoichiometric hydrogen and oxygen evolution in the pH range of 8–9. At pH values of 6.8 and 10, the rate of gas formation decreased significantly. To further assess the effect of pH on water splitting activity, an electrochemical analysis of YTOS at the solid/liquid interface was performed using particulate photoelectrodes prepared by the particle transfer method (Figure 3c). The MS plots acquired at different pH values (pH = 5.1, 6.8 and 13.0) all had positive slopes as the photoelectrode potential became more positive (Figure 15c). This outcome confirmed that YTOS is an n-type semiconductor. Interestingly, the E_{FB} value for YTOS was found to be −1.22 V vs. Ag/AgCl, irrespective of the pH of the electrolyte, in contrast to oxides and oxynitrides (such as $BaTaO_2N$, see Figure 12). Figure 15d presents a band energy diagram for YTOS for a pH of 9. Based on the E_g of 1.9 eV, the VBM and CBM were estimated to be located at approximately 0.9 V_{NHE} and −1.0 V_{NHE}, respectively. At a pH of 9, the CBM is more negative than the standard redox potential for the HER, while the VBM is located at a more positive position than the standard redox potential for the OER. However, the redox potentials for the HER and OER shift with changes in the solution pH at a rate of −59.2 mV/pH (representing a so-called Nernst shift). As such, at lower pH the potential (or overpotential) required for YTOS to promote the OER would be unfavorable. It should be noted that the gas evolution rates obtained using YTOS were balanced at the CBM and VBM positions against the standard redox potentials for the HER and OER.

The YTOS photocatalyst used in prior work was synthesized using a solid-state reaction (SSR) process that produced large particle sizes and structural defects. As noted with regard to the oxynitride photocatalyst $SrTaO_2N$, increases in the particle size increase the carrier transport distance, hence reducing activity because of carrier recombination. It is also helpful to reduce the concentration of defects in such materials so that carriers can be transported efficiently to the solid/liquid interface without trapping. There have been many attempts to control the particle size in this material through the use of molten salt fluxes, cation doping or the loading of optimized cocatalysts on the YTOS surface.[70] Recently, $Y_2Ti_2O_7$, Y_2O_2S and TiS_2 were found to be key intermediate phases in the formation of YTOS via the SSR technique.[71] By controlling the formation of these intermediates, it was found to be possible to prepare YTOS comprising smaller particles and with enhanced photocatalytic water splitting efficiency.

3.4.2. $La_5Ti_2(Cu,Ag)S_5O_7$ Photocatalysts

Work by Meigen et al. in 2004 demonstrated that $La_5Ti_2CuS_5O_7$ (LTC) and $La_5Ti_2AgS_5O_7$ (LTA) can function as oxysulfide semiconductor compounds possessing bandgap energies of 2.0 and 2.2 eV, respectively.[72] The absorption edge wavelength for LTC (approximately 620 nm) is longer than that for LTA (approximately 560 nm) due to a negative shift of the VBM resulting from the Cu 3d orbitals. Using density functional theory calculations, Brlec et al. established that one-dimensional octahedra of TiO_xS_{6-x} and tetragonal MS_4 (M = Cu or Ag) form channels that facilitate structural charge separation (Figures 16a–c)[73] and so reduce charge recombination. In addition, the analysis of needle-shaped single crystals of LTC has shown the existence of one-dimensional anisotropic electronic states along the *b*-axis.[74] Both LTC and LTA particles have a rod-like structure[75] and so anisotropic carrier transportation along the *b*-axis facilitates the electron transfer process (Figure 16d). A Pt cocatalyst was found to be selectively deposited on the edges of the LTC crystals when using a photo(electrochemical) deposition technique (Figure 16e).[76] This selective cocatalyst deposition suggested that charge carrier transfer was restricted to a one-dimensional process along the *b*-axis of each LTC particle. The selective cocatalyst loading (as opposed to random deposition) suggested that non-ideal cocatalysts could act as

© 2024 The Authors. ChemSusChem published by Wiley-VCH GmbH

1864564x, 2024, 21, Downloaded from https://chemistry-europe.onlinelibrary.wiley.com/doi/10.1002/cssc.202400663 by Turkey Cochrane Evidence Aid, Wiley Online Library on [04/09/2026]. See the Terms and Conditions (https://onlinelibrary.wiley.com/terms-and-conditions) on Wiley Online Library for rules of use; OA articles are governed by the applicable Creative Commons License

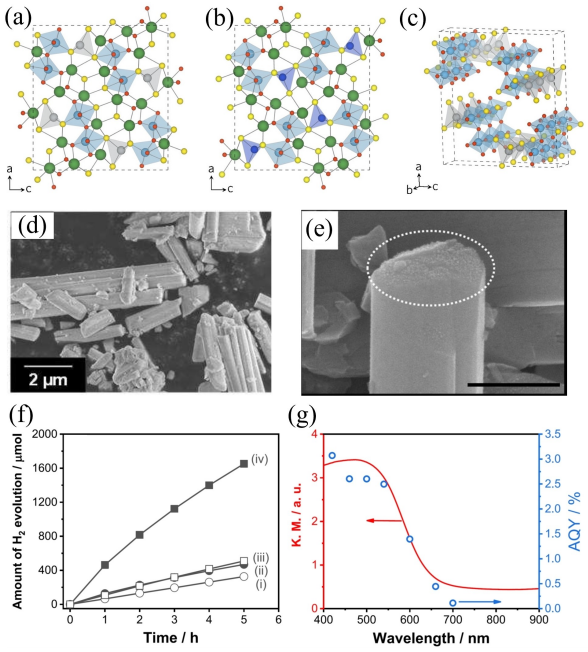

Figure 16. Photocatalytic water splitting on cation-doped $La_5Ti_2CuS_5O_7$ (LTC). The crystal structures of (a) $La_5Ti_2AgS_5O_7$ (LTA) and (b) LTC as seen along the b-axis. (c) One-dimensional tetrahedral and octahedral chains. La, Ti, S, O, Ag, Cu are colored in green, blue, yellow, red, silver, and dark blue, respectively. Adapted with permission from ref. [73]. Copyright 2022, American Chemical Society. (d) An SEM image of Ga-doped LTCA particles. Reproduced from ref. [75] with permission from the Royal Society of Chemistry. (e) An SEM image of Sc-doped LTC modified with a Pt cocatalyst. The dotted circle indicates the edge of the LTC with Pt nanoparticles having sizes of ~10 nm. Reproduced from ref. [76] with permission from the Royal Society of Chemistry. (f) Time course of hydrogen evolution (with a 300 W Xe lamp, $\lambda > 420$ nm) in an aqueous solution containing Na_2S (50 mM) and Na_2SO_3 (50 mM) using Ga-doped LTCA post-annealed at 473 K for 1 h in air (Ga-LTCA(S)) and without post-annealing (Ga-LTCA). (i) Rh(ph)/Ga-LTCA, (ii) Rh(ph)/Ga-LTCA(S), (iii) Rh(imp + ph)/Ga-LTCA, and (iv) Rh(imp + ph)/Ga-LTCA(S). (g) AQY as a function of wavelength during the HER using a Rh(imp + ph)/LTCA(S) photocatalyst. The solid red line shows the UV-visible diffuse reflectance spectrum of Ga-LTCA(S). Reproduced from ref. [80] with permission.

recombination centers for photogenerated carries (as in the case of IrO_x, see Figure 13). As such, the photocatalytic activity could be improved by optimizing the catalytic sites for the HER and OER.

Both LTC and LTA particles have been applied to photocatalytic water splitting in the presence of sacrificial reagents. LTC particles loaded with a Pt cocatalyst were shown to promote the HER half-reaction.[68] In addition, particulate photoelectrodes generated a cathodic photocurrent under visible light, as would be expected for a p-type semiconductor.[68] Doping with cations such as Sc^{3+} and Ga^{3+} at Ti^{4+} sites strengthened the p-type semiconductor characteristics of this material, resulting in enhanced HER activity.[77] Cation-doped LTC particulate photoelectrodes prepared via particle transfer provided an onset potential of approximately 0.9 V_{RHE}, which is one of the most positive onset potentials ever reported for a p-type semiconductor photoelectrode.[77] A positive onset potential for the HER is preferable with regard to the development of photocatalyst sheets for Z-scheme OWS (Figure 2c) or the design of a PEC cell for non-biased OWS (Figure 2d) when combined with n-type photocatalyst materials for the OER.

In trials using a solid solution of LTC and LTA ($La_5Ti_2Cu_{1-x}Ag_xS_5O_7$), the substitution of Ag atoms for 10% of the Cu ($La_5Ti_2Cu_{0.9}Ag_{0.1}S_5O_7$) shifted the absorption edge up to 710 nm.[69] However, with additional Ag substitution, the absorption edge wavelength was shortened. $La_5Ti_2Cu_{0.7}Ag_{0.3}S_5O_7$ showed an edge at 620 nm (the same as that for $La_5Ti_2CuS_5O_7$ without Ag substitution). A remaining challenge is that related to the lengths of LTCA particles. Using the conventional synthesis route based on an SSR process provides particles with lengths of 10–20 μm. These relatively long particles require charge carriers to migrate over significant distances to participate in photocatalytic reactions, which may limit the water splitting efficiency.

Improving carrier transport efficiency and reducing defects by decreasing the rod length of LTC and LTA particles are ongoing challenges. One approach to mitigate oxide impurities and defects is the addition of excess sulfur during the conventional SSR method.[78] Recent efforts have focused on the development of high quality oxysulfide photocatalysts by short thermal annealing to minimize surface and bulk defects. The flash sintering (FS) method has emerged as a promising technique for the preparation of high quality materials, allowing rapid synthesis by heat treatment within seconds.[79] A recent study by Cai et al. demonstrated that the FS method successfully produced LTA and LTC particles with shorter particle lengths and fewer defects compared to those synthesized by conventional SSR.[79a] Additionally, loading a Pt cocatalyst on the surface of the photocatalysts prepared by the FS method significantly enhanced the rate of photocatalytic HER half-reactions,[79a] outperforming samples prepared by the conventional SSR method. The controlled synthesis of oxysulfides with smaller particle sizes and fewer defects is expected to achieve efficient solar water splitting.

Pan et al. examined doping of LTCA with Ga together with thermal sulfidation to produce LTCA particles approximately 2 μm in length.[80] The pristine LTCA particles had a rod-like morphology but contained numerous burrs that had to be eliminated by annealing in the presence of sulfur vapor. In the presence of a sacrificial reagent, the HER rate was approximately seven times higher than that for a pristine LTCA sample (Figure 16f).[80] Optimization of the cocatalyst loading protocol also significantly improved the photocatalytic hydrogen evolution activity, and the AQY for the optimized LTCA particles reached 3.1% at 420 nm (Figure 16g). Furthermore, co-doping of LTCA with Ga^{3+} and Al^{3+} at Ti^{4+} sites effectively enhanced the HER rate, yielding an AQY of 18% at 420 nm.[81] The effects of cation doping, regulation of the particle length and modification with cocatalysts on water splitting efficiency were significant.

LTC and LTCA particulate materials have been employed as HER photocatalysts for two-step OWS on photocatalyst sheets.[15a,75,82] Recently, photocatalyst sheets composed of Mg,Al-codoped LTCA and Mo-doped $BiVO_4$ embedded in a thin Au conductive layer (Mg,Al-LCA/Au/Mo-$BiVO_4$) showed an AQY at 420 nm and STH efficiency of 16.3% and 0.67%,

© 2024 The Authors. ChemSusChem published by Wiley-VCH GmbH

1864564x, 2024, 21, Downloaded from https://chemistry-europe.onlinelibrary.wiley.com/doi/10.1002/cssc.202400663 by Turkey Cochrane Evidence Aid, Wiley Online Library on [04/09/2026]. See the Terms and Conditions (https://onlinelibrary.wiley.com/terms-and-conditions) on Wiley Online Library for rules of use; OA articles are governed by the applicable Creative Commons License

respectively.[83] A photocatalyst sheet having a Mg,Al-LTCA/Au/Mo-$BiVO_4$ structure exhibited stoichiometric hydrogen and oxygen evolution at wavelengths up to 700 nm. The use of photocatalysts sheets for OWS requires surface modification with appropriate cocatalysts and surface protection to enable selective hydrogen and oxygen evolution processes. The backward reaction and oxygen reduction reaction must also be suppressed. One successful photocatalyst sheet design uses core/shell type cocatalysts such as CrO_x/Rh or SiO_2/Rh[82b,83] to allow a selective HER process.

3.4.3. LTCA Particulate Photoelectrodes for PEC Cells Driving Non-Biased OWS

Surface coatings can improve the carrier transfer process while also providing long-term durability against photocorrosion (meaning self-photoreduction and photo-oxidation).[84] Such coatings will be required for further improvements in photocatalytic water splitting activity. Evaluating the semiconductor characteristics of photocatalysts can provide an in-depth understanding of the factors limiting photocatalytic OWS performance. In addition, quantifying the effects of surface modifications together with cation doping should provide rational guidelines for the future development of efficient photocatalytic water splitting systems.

As noted earlier, LTC-based particulate photoelectrodes have shown superior onset potentials in PEC HER processes. In addition, LTCA is a promising photoelectrode material that also exhibits an onset potential of 0.9 V_{RHE} for the HER.[69] Sc-doped LTC particulate photoelectrodes modified with a Pt cocatalyst provided a cathodic photocurrent density on the order of 0.2 mA cm^{-2} at 0.0 V_{RHE} under simulated AM 1.5G solar illumination.[77] In sharp contrast, Al-doped LTCA (Al-LTCA) modified with a Pt cocatalyst generated an enhanced cathodic photocurrent density of 1.0 mA cm^{-2} at 0.0 V_{RHE}. At 0.7 V_{RHE}, which is the typical working potential for a PEC cell comprising p-type and n-type semiconductor photoelectrodes, the cathodic photocurrent density generated by Pt/Al-LTCA was 0.2 mA cm^{-2} under simulated AM 1.5G solar illumination.[69] Comparing the PEC performance data for LTC and LTCA shows that the photocurrent density obtainable from Pt/Sc-LTC at 0.0 V_{RHE} is almost equivalent to the value for Pt/Al-LTCA at 0.7 V_{RHE} (which is more positive than 0.0 V_{RHE}). Since both electrodes used a Pt cocatalyst for the HER, the significant enhancement of the cathodic current derived from Al-LTCA has been attributed to Al-doping and Ag-substitution, which both promote the semiconducting nature of the material.

The effects of p-n junctions have been investigated as an approach to improving the HER performance of Al-LTCA particulate photoelectrodes. Prior work loaded this material with CdS using a chemical bath deposition method (otherwise referred to as a chemical bath treatment, CBT).[85] Al-LTCA treated with CdS in this manner and loaded with a Pt cocatalyst (Pt/CBT/Al-LTCA) provided a greater cathodic photocurrent density that was ascribed to improved electron transfer at the solid/liquid interface via the formation of p-n junctions. Surface protective layers based on oxides such as TiO_2, Nb_2O_5 and Ta_2O_5 have also been investigated as a means of improving durability.[85–86] The goal of providing surface protection to Al-LTCA particles was to achieve a high level of durability in any electrolyte, regardless of the pH of the aqueous solution. Figures 17a and 17b provide *J-E* and *J-t* curves for TiO_2-modified LTCA loaded with a Pt catalyst and coated with a CdS layer (denoted as Pt/TiO_2/CBT/Al-LTCA) as obtained at a pH of 13. Surface modification with TiO_2 and an ultrathin CdS layer evidently improved the photocurrent density and the durability of the catalyst during the HER process with exposure to light compared with Pt/Al-LTCA not having a surface protection layer. A parallel PEC cell combining Pt/TiO_2/CBT/LTCA:Al and Ir–Co modified $BaTaO_2N$ (Ir/Co/BTON) was able to produce hydrogen and oxygen at the expected stoichiometric ratio of 2:1 under simulated sunlight (AM 1.5G, 1 sun) without the application of an external bias voltage.[85] The Faradaic efficiency during non-biased OWS with this system was close to 100% and the STH efficiency of the parallel PEC cell was found to be 0.1%.

The TiO_2 coatings applied to LTCA particulate photocatalysts could be adapted for use in non-biased OWS with PEC cells in

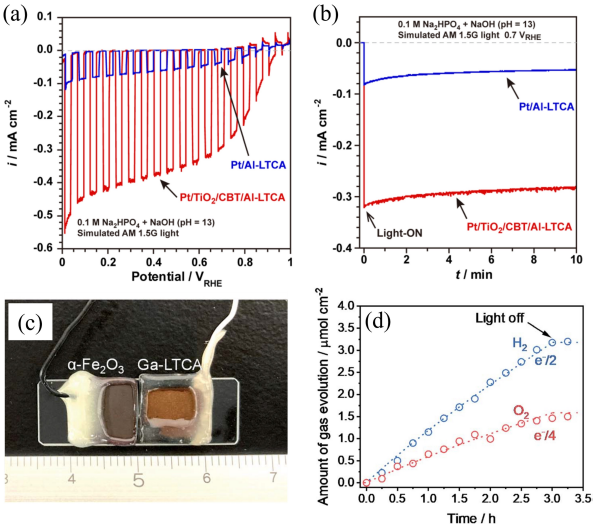

Figure 17. Effect of surface modification of a $La_5Ti_2Cu_{0.9}Ag_{0.1}S_5O_7$ (LTCA) photocatalyst on PEC performance. LTCA-based photoelectrodes were prepared through the particle transfer method. (a) photocurrent density-potential curves for Al-doped LTCA (Al-LTCA) modified with Pt (Pt/Al-LTCA, blue) and Pt/TiO_2/CdS (Pt/TiO_2/CBT/Al-LTCA, red) under chopped simulated AM 1.5G solar illumination. The electrolyte and potential sweep rate comprised a 0.1 M sodium phosphate aqueous solution with pH adjusted to 13 by the addition of NaOH and 10 mV s^{-1}, respectively. (b) Photocurrent density-time curves obtained from the particulate photoelectrodes at a constant photoelectrode potential of 0.7 V_{RHE} under continuous AM 1.5G solar illumination. Reproduced from ref. [85] with permission. (c) A photograph of a typical PEC cell consisting of an α-Fe_2O_3 particulate photoanode for the OER and a Ga-LTCA particulate photocathode for the HER. These two photoelectrodes were electrically connected through lead wires and placed side-by-side (parallel configuration). (d) The time course of non-biased OWS with a PEC cell based on a LTCA/Fe_2O_3 combination under simulated AM 1.5G solar illumination in a 0.1 M KP_i buffered aqueous solution (pH = 7.2). The symbols and dotted lines indicate the quantity of evolved gases and the values calculated from the photocurrent generated by the PEC cell, respectively. Reproduced from ref. [87] with permission from the Royal Society of Chemistry.

© 2024 The Authors. ChemSusChem published by Wiley-VCH GmbH

1864564x, 2024, 21, Downloaded from https://chemistry-europe.onlinelibrary.wiley.com/doi/10.1002/cssc.202400663 by Turkey Cochrane Evidence Aid, Wiley Online Library on [04/09/2026]. See the Terms and Conditions (https://onlinelibrary.wiley.com/terms-and-conditions) on Wiley Online Library for rules of use; OA articles are governed by the applicable Creative Commons License

neutral aqueous solutions. In prior work, a PEC cell containing LTCA (to promote the HER) and α-Fe_2O_3 (for the OER) was constructed (Figure 17c). This cell generated stoichiometric amounts of hydrogen and oxygen in a neutral solution.[87] The average rate of H_2 evolution over a 3 h trial was 1.05 μmol cm^{-2} h^{-1}, corresponding to an STH efficiency of 0.07% (Figure 17d). The STH efficiency of this LTCA-Fe_2O_3 combination was found to be similar to those reported for PEC cells employing a combination of LTCA/$BaTaO_2N$ (0.1%) and LTCA/Ta_3N_5 (0.2%).[85–88] However, it falls significantly short of the value of 10% required for practical applications. Nonetheless, it is evident that surface modification can promote OWS in neutral solutions, in contrast to the more common approach of using alkaline electrolytes (typically with a pH >9).[88] Such work demonstrates the progress to date in the design of visible-light-responsive particulate PEC water splitting systems operating with neutral electrolytes.

4. Summary and Outlook

This review summarized progress in photocatalytic water splitting to produce green hydrogen using solar energy and water as resources. Green hydrogen can also be produced by the electrolysis of water using electricity obtained from solar cells or solar thermal power generation. If the STH energy conversion efficiency can be increased to a level comparable to that obtainable from photovoltaic-assisted water electrolysis, photocatalytic hydrogen production could be deployed in large-scale plants and the use of photocatalytic panels can be expected to reduce costs. Materials that can utilize wavelengths greater than 600 nm for photocatalytic OWS have been reported, as described herein, and green hydrogen production using particulate photocatalysts and photoelectrodes could be further improved to allow greater STH energy conversion efficiencies.

Achieving a high level of STH energy conversion efficiency and realizing a practical photocatalytic water splitting system remains challenging. Despite the capability of particulate photocatalysts to drive OWS through one-step and two-step photoexcitation processes, the latest STH energy conversion efficiencies of photocatalytic one-step OWS are below 1%. Developing more efficient particulate photocatalyst materials is essential for achieving high level of STH energy conversion efficiency for practical green hydrogen production. This review article aims to provide researchers across various fields with a deeper understanding of the potential impact of photocatalytic water splitting, thereby contributing to innovative concepts and advanced technologies to overcome the current limitations on STH efficiency in photocatalytic OWS.

Future research directions can be outlined as follows. Improving the bulk semiconductor properties of particulate photocatalysts is crucial. Reducing the recombination of excited carriers by improving the crystallinity associated with carrier concentration and mobility is essential. Investigating the effects of photocatalyst preparation methods to improve particle crystallinity, including facet engineering using flux salts and rapid synthesis techniques, would be promising. As described previously, cation doping and precursor exploration are considered to be effective for high quality visible-light-absorbing photocatalyst materials.

Optimization of the solid/liquid interface structure through surface design of particulate photocatalysts is necessary. Efficient transport of the generated carriers to the catalytic site, in particular to the cocatalyst/water interface, requires careful study of the state of the photocatalyst/cocatalyst interface and maximization of the electrocatalytic performance of the cocatalysts. Although the water splitting activity of some cocatalyst materials has been evaluated, further progress should be made in the electrochemical investigation of the electrocatalytic properties of cocatalysts to obtain the rational guidelines for interface design.

Investigations into photocatalysis are intricately intertwined with the quest to discern active species and sites, with the aim of promoting specific reaction processes. The development of photocatalysts for solar-to-chemical energy conversion will require an understanding of the behavior of photoexcited carriers, given that photocatalysis involves a sequence of events unfolding under non-equilibrium conditions. In particular, these events involve photoexcited carriers having finite lifetimes. Consequently, analytical techniques providing good temporal resolution have assumed a pivotal role. TAS has been employed to assess carrier dynamics in photocatalysts and the impact of cocatalyst loading.[89] Carrier dynamics have been found to be profoundly influenced by the immediate environment, especially in aqueous solutions. Hence, *in situ* (operando) analytical techniques examining photoexcitation in aqueous solutions will be indispensable for investigating the intrinsic characteristics of photocatalysts.[90]

Moreover, it has become evident that the chemical states of cocatalysts might differ between dark and illuminated conditions due to the presence of photoexcited carriers.[91] These findings have been prominently addressed in recent years in the investigation of single atom (co)catalysts on photocatalysis. For instance, Zhang et al demonstrated notable findings on carrier transfer and chemical bond structure of single-atom Pt cocatalyst loaded on C_3N_4 photocatalyst using *in situ* XPS with synchronous light illumination.[91c] Under light excitation, the Pt–N bond cleavages to form Pt^0 species along with the reconstruction of the C=N bond.[91c] The emergence of Pt^0 might act as a catalytic site for HER, enhancing photocatalytic water splitting activity. T.-Kiakalaieh et al. reported that single-atom Ru cocatalyst incorporating CdS quantum dots exhibit an accumulation of excited carriers from the bulk to the Ru atoms, increasing the distribution of photo-excited electrons across the surface, as revealed by quasi *in situ* XPS.[92] In the case of the PEC system, Dahl et al. successfully observed Fermi-level pinning of NiO_x-coated Ta_3N_5 (n-type semiconductor) in contact with aqueous solutions under both dark and light illumination conditions using the operando ambient pressure XPS techniques.[93] They suggest that surface passivation of defect states responsible for Fermi level pinning in Ta_3N_5 can suppress carrier recombination by unpinning the quasi-Fermi level of

© 2024 The Authors. ChemSusChem published by Wiley-VCH GmbH

1864564x, 2024, 21, Downloaded from https://chemistry-europe.onlinelibrary.wiley.com/doi/10.1002/cssc.202400663 by Turkey Cochrane Evidence Aid, Wiley Online Library on [04/09/2026]. See the Terms and Conditions (https://onlinelibrary.wiley.com/terms-and-conditions) on Wiley Online Library for rules of use; OA articles are governed by the applicable Creative Commons License

photogenerated holes, thus enabling efficient and stable PEC water splitting.[93]

Direct potential measurements represent a useful means of gaining insights into the physicochemical properties of cocatalysts loaded on particulate photocatalysts during irradiation. At present, photogenerated electrons generated in particulate photocatalysts dispersed in aqueous solutions are typically monitored using reference electrodes that collect electrons from the various particles.[94] *In situ* analyses using PEC systems based on photoelectrodes represent another promising technique. Several studies have attempted to measure the cocatalyst potential or surface potential of photocatalysts. Boettcher et al. employed a double working electrode system to ascertain the surface potentials of OER cocatalysts such as IrO_x and NiO_x loaded on a TiO_2 photoelectrode.[95] Investigations using surface probe microscopy techniques (such as atomic force and Kelvin probe microscopy) to determine the electrochemical potentials of cocatalysts on photoelectrodes have also provided useful information concerning electric power output.[96] Visualizing the carrier transfer processes on photocatalysts can also elucidate time-resolved carrier dynamics and spatial charge separation occurring during photocatalysis, providing rational guidelines for the design of efficient (photo)catalytic sites.[97]

Ensuring the long-term stability of OWS photocatalysts is essential. Activity testing in the presence of sacrificial reagents (electron donor and acceptor) provides useful information about photocatalyst properties. However, the goal is to achieve OWS from pure water without the sacrificial reagents. Achieving long-term stability requires the chemical stability of the photocatalyst materials as well as the chemical durability of the cocatalysts both in the dark and under light illumination conditions. Appropriate surface modification is expected to be necessary to prevent dissolution or detachment of the cocatalysts from the photocatalyst surface. Further studies need to be conducted in the future to realize efficient and durable photocatalytic hydrogen production required for commercialization.

Since the water splitting reaction produces a mixture of hydrogen and oxygen, it is necessary to safely separate the former product. It should be emphasized that gas separation technologies are also currently being developed. As an example, an outdoor 100 m^2-scale photocatalytic plant is described herein. It is expected that continued research and development will further improve the performance of photocatalysts to realize the high levels of STH efficiency required for practical commercial applications.

Acknowledgements

We thank the editor of this journal for kindly inviting the submission of this paper. This work was financially supported by the Artificial Photosynthesis Project via the New Energy and Industrial Technology Development Organization (NEDO) and by a Grant-in-Aid for Scientific Research (C) (no. 23K04917) from the Japan Society for the Promotion of Science (JSPS).

Conflict of Interests

The authors declare no conflict of interest.

Data Availability Statement

The data that support the findings of this study are available from the corresponding author upon reasonable request.

Keywords: Energy Conversion · Hydrogen · Photocatalyst · Photoelectrochemistry · Water Splitting

[1] a) A. Kudo, Y. Miseki, *Chem. Soc. Rev.* **2009**, *38*, 253–278; b) M. G. Walter, E. L. Warren, J. R. McKone, S. W. Boettcher, Q. Mi, E. A. Santori, N. S. Lewis, *Chem. Rev.* **2010**, *110*, 6446–6473; c) T. Hisatomi, J. Kubota, K. Domen, *Chem. Soc. Rev.* **2014**, *43*, 7520–7535; d) S. Nandy, S. A. Savant, S. Haussener, *Chem. Sci.* **2021**, *12*, 9866–9884; e) A. Vilanova, P. Dias, T. Lopes, A. Mendes, *Chem. Soc. Rev.* **2024**, *53*, 2388–2434.
[2] a) K. Takanabe, *ACS Catal.* **2017**, *7*, 8006–8022; b) T. Hisatomi, K. Domen, *Nat. Catal.* **2019**, *2*, 387–399; c) K. Maeda, *ACS Catal.* **2013**, *3*, 1486–1503; d) R. Abe, *J. Photochem. Photobiol. C* **2010**, *11*, 179–209.
[3] a) H. Nishiyama, T. Yamada, M. Nakabayashi, Y. Maehara, M. Yamaguchi, Y. Kuromiya, Y. Nagatsuma, H. Tokudome, S. Akiyama, T. Watanabe, R. Narushima, S. Okunaka, N. Shibata, T. Takata, T. Hisatomi, K. Domen, *Nature* **2021**, *598*, 304–307; b) Y. Goto, T. Hisatomi, Q. Wang, T. Higashi, K. Ishikiriyama, T. Maeda, Y. Sakata, S. Okunaka, H. Tokudome, M. Katayama, S. Akiyama, H. Nishiyama, Y. Inoue, T. Takewaki, T. Setoyama, T. Minegishi, T. Takata, T. Yamada, K. Domen, *Joule* **2018**, *2*, 509–520.
[4] A. Fujishima, K. Honda, *Nature* **1972**, *238*, 37–38.
[5] a) A. Fujishima, X. Zhang, D. A. Tryk, *Surf. Sci. Rep.* **2008**, *63*, 515–582; b) M. N. Chong, B. Jin, C. W. K. Chow, C. Saint, *Water Res.* **2010**, *44*, 2997–3027.
[6] a) K. Domen, S. Naito, M. Soma, T. Onishi, K. Tamaru, *J. Chem. Soc. Chem. Commun.* **1980**, 543–544; b) S. Sato, J. M. White, *Chem. Phys. Lett.* **1980**, *72*, 83–86.
[7] F. E. Osterloh, *ACS Energy Lett.* **2017**, *2*, 445–453.
[8] a) M. Grätzel, *Nature* **2001**, *414*, 338–344; b) K. Sivula, R. van de Krol, *Nat. Rev. Mater.* **2016**, *1*, 15010.
[9] a) Y. Kawase, T. Higashi, K. Domen, K. Takanabe, *Adv. Energy Sustainability Res.* **2021**, *2*, 2100023; b) Y. Kuang, T. Yamada, K. Domen, *Joule* **2017**, *1*, 290–305.
[10] Y. Wang, H. Suzuki, J. Xie, O. Tomita, D. J. Martin, M. Higashi, D. Kong, R. Abe, J. Tang, *Chem. Rev.* **2018**, *118*, 5201–5241.
[11] a) M. Sakar, R. M. Prakash, K. Shinde, G. R. Balakrishna, *Int. J. Hydrogen Energy* **2020**, *45*, 7691–7705; b) W.-J. Chun, A. Ishikawa, H. Fujisawa, T. Takata, J. N. Kondo, M. Hara, M. Kawai, Y. Matsumoto, K. Domen, *J. Phys. Chem. B* **2003**, *107*, 1798–1803.
[12] a) V. Nandal, Y. Pihosh, T. Higashi, T. Minegishi, T. Yamada, K. Seki, M. Sugiyama, K. Domen, *Energy Environ. Sci.* **2021**, *14*, 4038–4047; b) T. Higashi, H. Nishiyama, V. Nandal, Y. Pihosh, Y. Kawase, R. Shoji, M. Nakabayashi, Y. Sasaki, N. Shibata, H. Matsuzaki, K. Seki, K. Takanabe, K. Domen, *Energy Environ. Sci.* **2022**, *15*, 4761–4775; c) T. Higashi, H. Nishiyama, Y. Pihosh, K. Wakishima, Y. Kawase, Y. Sasaki, A. Nagaoka, K. Yoshino, K. Takanabe, K. Domen, *Phys. Chem. Chem. Phys.* **2023**, *25*, 20737–20748; d) T. Higashi, H. Nishiyama, Y. Otsuka, Y. Kawase, Y. Sasaki, M. Nakabayashi, M. Katayama, T. Minegishi, N. Shibata, K. Takanabe, T. Yamada, K. Domen, *ChemSusChem* **2020**, *13*, 1974–1978.
[13] a) B. A. Pinaud, J. D. Benck, L. C. Seitz, A. J. Forman, Z. Chen, T. G. Deutsch, B. D. James, K. N. Baum, G. N. Baum, S. Ardo, H. Wang, E. Miller, T. F. Jaramillo, *Energy Environ. Sci.* **2013**, *6*, 1983–2002; b) M. R. Shaner, H. A. Atwater, N. S. Lewis, E. W. McFarland, *Energy Environ. Sci.* **2016**, *9*, 2354–2371.
[14] a) M. Qureshi, K. Takanabe, *Chem. Mater.* **2017**, *29*, 158–167; b) K. Takanabe, in *Solar Energy for Fuels* (Eds.: H. Tüysüz, C. K. Chan), Springer International Publishing, Cham, **2016**, pp. 73–103.
[15] a) S. Nandy, T. Hisatomi, T. Takata, T. Setoyama, K. Domen, *J. Mater. Chem. A* **2023**, *11*, 20470–20479; b) Q. Wang, T. Hisatomi, M. Katayama, T. Takata, T. Minegishi, A. Kudo, T. Yamada, K. Domen, *Faraday Discuss.* **2017**, *197*, 491–504; c) T. Higashi, H. Kaneko, T. Minegishi, H. Kobayashi,

© 2024 The Authors. ChemSusChem published by Wiley-VCH GmbH

1864564x, 2024, 21, Downloaded from https://chemistry-europe.onlinelibrary.wiley.com/doi/10.1002/cssc.202400663 by Turkey Cochrane Evidence Aid, Wiley Online Library on [04/09/2026]. See the Terms and Conditions (https://onlinelibrary.wiley.com/terms-and-conditions) on Wiley Online Library for rules of use; OA articles are governed by the applicable Creative Commons License

M. Zhong, Y. Kuang, T. Hisatomi, M. Katayama, T. Takata, H. Nishiyama, T. Yamada, K. Domen, *Chem. Commun.* **2017**, *53*, 11674–11677.
[16] G. Askarova, C. Xiao, K. Barman, X. Wang, L. Zhang, F. E. Osterloh, M. V. Mirkin, *J. Am. Chem. Soc.* **2023**, *145*, 6526–6534.
[17] a) Q. Wang, Y. Li, T. Hisatomi, M. Nakabayashi, N. Shibata, J. Kubota, K. Domen, *J. Catal.* **2015**, *328*, 308–315; b) Q. Wang, T. Hisatomi, Q. Jia, H. Tokudome, M. Zhong, C. Wang, Z. Pan, T. Takata, M. Nakabayashi, N. Shibata, Y. Li, I. D. Sharp, A. Kudo, T. Yamada, K. Domen, *Nat. Mater.* **2016**, *15*, 611–615; c) Q. Wang, T. Hisatomi, Y. Suzuki, Z. Pan, J. Seo, M. Katayama, T. Minegishi, H. Nishiyama, T. Takata, K. Seki, A. Kudo, T. Yamada, K. Domen, *J. Am. Chem. Soc.* **2017**, *139*, 1675–1683; d) Q. Wang, S. Okunaka, H. Tokudome, T. Hisatomi, M. Nakabayashi, N. Shibata, T. Yamada, K. Domen, *Joule* **2018**, *2*, 2667–2680.
[18] a) K.-H. Dahmen, in *Encyclopedia of Physical Science and Technology (Third Edition)* (Ed.: R. A. Meyers), Academic Press, New York, **2003**, pp. 787–808; b) J. Musil, P. Baroch, J. Vlček, K. H. Nam, J. G. Han, *Thin Solid Films* **2005**, *475*, 208–218; c) L.-j. Meng, M. P. dos Santos, *Thin Solid Films* **1998**, *322*, 56–62.
[19] a) C. Zhen, X. Chen, R. Chen, F. Fan, X. Xu, Y. Kang, J. Guo, L. Wang, G. Q. Lu, K. Domen, H.-M. Cheng, G. Liu, *Nat. Commun.* **2024**, *15*, 1672; b) X. Xiao, M. Iwase, G. Yin, M. Nakabayashi, T. Higashi, N. Shibata, K. Domen, T. Watanabe, *ACS Sustainable Chem. Eng.* **2019**, *7*, 19407–19414.
[20] a) M. Higashi, K. Domen, R. Abe, *Energy Environ. Sci.* **2011**, *4*, 4138–4147; b) X. Guo, X. Li, C. Lai, W. Li, D. Zhang, Z. Xiong, *Appl. Surf. Sci.* **2015**, *331*, 455–462; c) M. Kim, B. Lee, H. Ju, J. Y. Kim, J. Kim, S. W. Lee, *Adv. Mater.* **2019**, *31*, 1903316; d) S. Obregón, G. Amor, A. Vázquez, *Adv. Colloid Interface Sci.* **2019**, *269*, 236–255; e) R. Ghosh, R. P. Sahu, R. Ganguly, I. Zhitomirsky, I. K. Puri, *Ceram. Int.* **2020**, *46*, 3777–3785; f) K. Atacan, N. Güy, B. Boutra, M. Özacar, *Int. J. Hydrogen Energy* **2020**, *45*, 17453–17467; g) J. Seo, S. Jeong, S. Kim, *ACS Appl. Energ. Mater.* **2021**, *4*, 3141–3150.
[21] a) Y. Asakura, Y. Nishimura, Y. Masubuchi, S. Yin, *Eur. J. Inorg. Chem.* **2019**, *2019*, 1999–2005; b) H. V. Le, P. T. Pham, L. T. Le, A. D. Nguyen, N. Q. Tran, P. D. Tran, *Int. J. Hydrogen Energy* **2021**, *46*, 22852–22863; c) F. Tulli, J. M. N. Morales, E. E. Salas, F. E. Morán Vieyra, C. D. Borsarelli, *Photochem. Photobiol.* **2021**, *97*, 22–31.
[22] T. Minegishi, N. Nishimura, J. Kubota, K. Domen, *Chem. Sci.* **2013**, *4*, 1120–1124.
[23] a) P. An, B. Yang, N. Zhang, H. Li, M. Liu, *Transp. Saf. Environ.* **2020**, *1*, 212–219; b) Y. Kuang, Q. Jia, G. Ma, T. Hisatomi, T. Minegishi, H. Nishiyama, M. Nakabayashi, N. Shibata, T. Yamada, A. Kudo, K. Domen, *Nat. Energy* **2016**, *2*, 16191; c) H. Fukai, K. Nagatsuka, Y. Yamaguchi, A. Iwase, A. Kudo, *ECS J. Solid State Sci. Technol.* **2022**; d) R. Mizuochi, N. Hirayama, K. Maeda, *J. Phys. Chem. C* **2023**; e) Y. Asakura, T. Higashi, H. Nishiyama, H. Kobayashi, M. Nakabayashi, N. Shibata, T. Minegishi, T. Hisatomi, M. Katayama, T. Yamada, K. Domen, *Sustain. Energy Fuels* **2018**, *2*, 73–78.
[24] Y. Sakata, T. Hayashi, R. Yasunaga, N. Yanaga, H. Imamura, *Chem. Commun.* **2015**, *51*, 12935–12938.
[25] T. Takata, J. Jiang, Y. Sakata, M. Nakabayashi, N. Shibata, V. Nandal, K. Seki, T. Hisatomi, K. Domen, *Nature* **2020**, *581*, 411–414.
[26] K. Maeda, K. Domen, *J. Phys. Chem. Lett.* **2010**, *1*, 2655–2661.
[27] C. Pan, T. Takata, M. Nakabayashi, T. Matsumoto, N. Shibata, Y. Ikuhara, K. Domen, *Angew. Chem. Int. Ed.* **2015**, *54*, 2955–2959.
[28] Z. Wang, Y. Inoue, T. Hisatomi, R. Ishikawa, Q. Wang, T. Takata, S. Chen, N. Shibata, Y. Ikuhara, K. Domen, *Nat. Catal.* **2018**, *1*, 756–763.
[29] Q. Wang, M. Nakabayashi, T. Hisatomi, S. Sun, S. Akiyama, Z. Wang, Z. Pan, X. Xiao, T. Watanabe, T. Yamada, N. Shibata, T. Takata, K. Domen, *Nat. Mater.* **2019**, *18*, 827–832.
[30] T. Hisatomi, K. Takanabe, K. Domen, *Catal. Lett.* **2015**, *145*, 95–108.
[31] a) Y. Zhang, X. Wu, Z.-H. Wang, Y. Peng, Y. Liu, S. Yang, C. Sun, X. Xu, X. Zhang, J. Kang, S.-H. Wei, P. F. Liu, S. Dai, H. G. Yang, *J. Am. Chem. Soc.* **2024**; b) Y. Qin, F. Fang, Z. Xie, H. Lin, K. Zhang, X. Yu, K. Chang, *ACS Catal.* **2021**, *11*, 11429–11439; c) Y.-G. Lee, Y.-C. Cheng, Y.-T. Lin, J. C. S. Wu, W.-Y. Yu, M. M. Kržmanc, S. Gupta, E. Kotomin, *J. Phys. Chem. C* **2023**, *127*, 9981–9991; d) Y. Ham, T. Hisatomi, Y. Goto, Y. Moriya, Y. Sakata, A. Yamakata, J. Kubota, K. Domen, *J. Mater. Chem. A* **2016**, *4*, 3027–3033.
[32] a) Y. Wang, W. Ma, Y. Song, J. Chen, J. Xu, D. Wang, Z. Mao, *J. Rare Earth.* **2021**, *39*, 541–547; b) S. Ikeda, R. Okamoto, A. Kimura, Y. Nakayasu, A. Yamakata, R. Tomizawa, T. Masuda, K. Nakatani, *Sustain. Energy Fuels* **2024**, *8*, 202–209; c) S. Kawasaki, R. Takahashi, K. Akagi, J. Yoshinobu, F. Komori, K. Horiba, H. Kumigashira, K. Iwashina, A. Kudo, M. Lippmaa, *J. Phys. Chem. C* **2014**, *118*, 20222–20228.
[33] a) H. Lyu, T. Hisatomi, Y. Goto, M. Yoshida, T. Higashi, M. Katayama, T. Takata, T. Minegishi, H. Nishiyama, T. Yamada, Y. Sakata, K. Asakura, K. Domen, *Chem. Sci.* **2019**, *10*, 3196–3201; b) C. Pornrungroj, A. B. Mohamad Annuar, Q. Wang, M. Rahaman, S. Bhattacharjee, V. Andrei, E. Reisner, *Nat. Water* **2023**, *1*, 952–960; c) T. Suguro, F. Kishimoto, N. Kariya, T. Fukui, M. Nakabayashi, N. Shibata, T. Takata, K. Domen, K. Takanabe, *Nat. Commun.* **2022**, *13*, 5698.
[34] S. Assavachin, C. Xiao, K. Becker, F. E. Osterloh, *Energy Environ. Sci.* **2024**. (DOI: 10.1039/D3EE04308H).
[35] Y. Ham, T. Minegishi, T. Hisatomi, K. Domen, *Chem. Commun.* **2016**, *52*, 5011–5014.
[36] a) S. Patial, V. Hasija, P. Raizada, P. Singh, A. A. P. Khan Singh, A. M. Asiri, *J. Environ. Chem. Eng.* **2020**, *8*, 103791; b) R. Konta, T. Ishii, H. Kato, A. Kudo, *J. Phys. Chem. B* **2004**, *108*, 8992–8995; c) T. Ishii, H. Kato, A. Kudo, *J. Photochem. Photobiol. A: Chem.* **2004**, *163*, 181–186; d) K. Furuhashi, Q. Jia, A. Kudo, H. Onishi, *J. Phys. Chem. Chem. Phys.* **2013**, *117*, 19101–19106; e) D. H. K. Murthy, H. Matsuzaki, Q. Wang, Y. Suzuki, K. Seki, T. Hisatomi, T. Yamada, A. Kudo, K. Domen, A. Furube, *Sustain. Energy Fuels* **2019**, *3*, 208–218.
[37] Q. Wang, T. Hisatomi, S. S. K. Ma, Y. Li, K. Domen, *Chem. Mater.* **2014**, *26*, 4144–4150.
[38] a) Y. Lee, H. Terashima, Y. Shimodaira, K. Teramura, M. Hara, H. Kobayashi, K. Domen, M. Yashima, *J. Phys. Chem. C* **2007**, *111*, 1042–1048; b) Y. Lee, K. Teramura, M. Hara, K. Domen, *Chem. Mater.* **2007**, *19*, 2120–2127; c) K. Maeda, K. Teramura, D. Lu, T. Takata, N. Saito, Y. Inoue, K. Domen, *Nature* **2006**, *440*, 295–295; d) K. Maeda, T. Takata, M. Hara, N. Saito, Y. Inoue, H. Kobayashi, K. Domen, *J. Am. Chem. Soc.* **2005**, *127*, 8286–8287.
[39] Z. Zhang, B. Huang, Q. Qian, Z. Gao, X. Tang, B. Li, *APL Mater.* **2020**, *8*.
[40] a) M. Saruyama, C. M. Pelicano, T. Teranishi, *Chem. Sci.* **2022**, *13*, 2824–2840; b) R. Li, F. Zhang, D. Wang, J. Yang, M. Li, J. Zhu, X. Zhou, H. Han, C. Li, *Nat. Commun.* **2013**, *4*, 1432; c) H. Kaneko, T. Minegishi, T. Higashi, M. Nakabayashi, N. Shibata, K. Domen, *Small Methods* **2018**, *2*, 1800018.
[41] a) T. Nishino, M. Saruyama, Z. Li, Y. Nagatsuma, M. Nakabayashi, N. Shibata, T. Yamada, R. Takahata, S. Yamazoe, T. Hisatomi, K. Domen, T. Teranishi, *Chem. Sci.* **2020**, *11*, 6862–6867; b) W. Kurashige, Y. Mori, S. Ozaki, M. Kawachi, S. Hossain, T. Kawawaki, C. J. Shearer, A. Iwase, G. F. Metha, S. Yamazoe, A. Kudo, Y. Negishi, *Angew. Chem. Int. Ed.* **2020**, *59*, 7076–7082.
[42] a) W. Liu, X. Wang, H. Yu, J. Yu, *ACS Sustainable Chem. Eng.* **2018**, *6*, 12436–12445; b) X. Lu, C. Y. Toe, F. Ji, W. Chen, X. Wen, R. J. Wong, J. Seidel, J. Scott, J. N. Hart, Y. H. Ng, *ACS Appl. Mater. Interfaces* **2020**, *12*, 8324–8332; c) T. Di, B. Zhu, J. Zhang, B. Cheng, J. Yu, *Appl. Surf. Sci.* **2016**, *389*, 775–782.
[43] K. Maeda, K. Teramura, D. Lu, N. Saito, Y. Inoue, K. Domen, *Angew. Chem. Int. Ed.* **2006**, *45*, 7806–7809.
[44] M. Yoshida, K. Takanabe, K. Maeda, A. Ishikawa, J. Kubota, Y. Sakata, Y. Ikezawa, K. Domen, *J. Phys. Chem. C* **2009**, *113*, 10151–10157.
[45] T. Higashi, K. Seki, Y. Sasaki, Y. Pihosh, V. Nandal, M. Nakabayashi, N. Shibata, K. Domen, *Chem. Eur. J.* **2023**, *29*, e202204058.
[46] a) M. Yoshida, K. Maeda, D. Lu, J. Kubota, K. Domen, *J. Phys. Chem. C* **2013**, *117*, 14000–14006; b) A. T. Garcia-Esparza, T. Shinagawa, S. Ould-Chikh, M. Qureshi, X. Peng, N. Wei, D. H. Anjum, A. Clo, T.-C. Weng, D. Nordlund, D. Sokaras, J. Kubota, K. Domen, K. Takanabe, *Angew. Chem. Int. Ed.* **2017**, *56*, 5780–5784; c) J. A. Bau, K. Takanabe, *ACS Catal.* **2017**, *7*, 7931–7940; d) T. H. Chiang, H. Lyu, T. Hisatomi, Y. Goto, T. Takata, M. Katayama, T. Minegishi, K. Domen, *ACS Catal.* **2018**, *8*, 2782–2788; e) Z. Li, R. Li, H. Jing, J. Xiao, H. Xie, F. Hong, N. Ta, X. Zhang, J. Zhu, C. Li, *Nat. Catal.* **2023**, *6*, 80–88; f) S. Okunaka, H. Kameshige, T. Ikeda, H. Tokudome, T. Hisatomi, T. Yamada, K. Domen, *ChemSusChem* **2020**, *13*, 4906–4910.
[47] a) T. Yamada, Y. Murata, S. Suzuki, H. Wagata, S. Oishi, K. Teshima, *J. Phys. Chem. Chem. Phys.* **2018**, *122*, 8037–8044; b) L. Yang, Z. Li, X. Xu, *Appl. Catal. B* **2024**, *340*, 123221.
[48] a) G. Lin, R. Wang, T. Cao, L. Yuan, X. Xu, *Inorg. Chem. Front.* **2020**, *7*, 2629–2636; b) S. Wang, Y. Bao, Y. Qi, H. Zou, S. Du, X. Xin, N. Yang, C. Yang, Q.-l. Wang, F. Zhang, *Energy Fuels* **2022**, *36*, 11477–11484; c) X. Sun, G. Liu, X. Xu, *J. Mater. Chem.* **2018**, *6*, 10947–10957.
[49] a) X. Wang, T. Hisatomi, J. Liang, Z. Wang, Y. Xiang, Y. Zhao, X. Dai, T. Takata, K. Domen, *J. Mater. Chem.* **2020**, *8*, 11743–11751; b) J. Yu, X. Xu, *J. Catal.* **2022**, *413*, 858–869; c) J. Seo, *Bull. Korean Chem. Soc.* **2021**, *42*, 571–576.
[50] a) F. Zhang, A. Yamakata, K. Maeda, Y. Moriya, T. Takata, J. Kubota, K. Teshima, S. Oishi, K. Domen, *J. Am. Chem.* **2012**, *134*, 8348–8351; b) F.

© 2024 The Authors. ChemSusChem published by Wiley-VCH GmbH

1864564x, 2024, 21, Downloaded from https://chemistry-europe.onlinelibrary.wiley.com/doi/10.1002/cssc.202400663 by Turkey Cochrane Evidence Aid, Wiley Online Library on [04/09/2026]. See the Terms and Conditions (https://onlinelibrary.wiley.com/terms-and-conditions) on Wiley Online Library for rules of use; OA articles are governed by the applicable Creative Commons License

Wu, G. Liu, X. Xu, *J. Catal.* **2017**, *346*, 10–20; c) G. Lin, X. Sun, X. Xu, *Appl. Catal. B* **2023**, *324*, 122258.
[51] M. Hara, G. Hitoki, T. Takata, J. N. Kondo, H. Kobayashi, K. Domen, *Catal. Today* **2003**, *78*, 555–560.
[52] a) X. Jia, C. Wang, Y. Li, R. Zhang, Z. Shi, X. Liu, X. Yu, M. Zhang, Y. Xing, *Chem. Eng. J.* **2022**, *431*, 134041; b) J. Cui, Y. Qi, B. Dong, L. Mu, Q. Ding, G. Liu, M. Jia, F. Zhang, C. Li, *Appl. Catal. B* **2019**, *241*, 1–7; c) S. S. K. Ma, K. Maeda, T. Hisatomi, M. Tabata, A. Kudo, K. Domen, *Chem. Eur. J.* **2013**, *19*, 7480–7486; d) Q. Wang, T. Hisatomi, S. S. K. Ma, Y. Li, K. Domen, *Chem. Mater.* **2014**, *26*, 4144–4150.
[53] Y. Qi, S. Chen, M. Li, Q. Ding, Z. Li, J. Cui, B. Dong, F. Zhang, C. Li, *Chem. Sci.* **2017**, *8*, 437–443.
[54] a) M. Hojamberdiev, J. M. Mora-Hernandez, R. Vargas, A. Yamakata, K. Yubuta, E. M. Heppke, L. M. Torres-Martínez, K. Teshima, M. Lerch, *ACS Appl. Energ. Mater.* **2021**, *4*, 9315–9327; b) A. Hosono, Y. Masubuchi, S. Yasui, M. Takesada, T. Endo, M. Higuchi, M. Itoh, S. Kikkawa, *Inorg. Chem.* **2019**, *58*, 16752–16760.
[55] a) M. Hojamberdiev, R. Vargas, Z. C. Kadirova, K. Kato, H. Sena, A. G. Krasnov, A. Yamakata, K. Teshima, M. Lerch, *ACS Catal.* **2022**, *12*, 1403–1414; b) H. Zhang, S. Wei, X. Xu, *J. Catal.* **2020**, *383*, 135–143; c) Z. Lan, T. Vegge, I. E. Castelli, *Chem. Mater.* **2021**, *33*, 3297–3303; d) S. Wei, G. Zhang, X. Xu, *Appl. Catal. B* **2018**, *237*, 373–381; e) H. Li, J. J. M. Vequizo, T. Hisatomi, M. Nakabayashi, J. Xiao, X. Tao, Z. Pan, W. Li, S. Chen, Z. Wang, N. Shibata, A. Yamakata, T. Takata, K. Domen, *EES Catal.* **2023**, *1*, 26–35.
[56] a) H. Okamoto, M. Kodera, T. Hisatomi, M. Katayama, T. Minegishi, K. Domen, *Catal. Today* **2020**, *354*, 204–210; b) Z. Wang, Y. Luo, T. Hisatomi, J. J. M. Vequizo, S. Suzuki, S. Chen, M. Nakabayashi, L. Lin, Z. Pan, N. Kariya, A. Yamakata, N. Shibata, T. Takata, K. Teshima, K. Domen, *Nat. Commun.* **2021**, *12*, 1005.
[57] a) J. Abdul Nasir, A. Munir, N. Ahmad, T. u. Haq, Z. Khan, Z. Rehman, *Adv. Mater.* **2021**, *33*, 2105195; b) M. Higashi, R. Abe, T. Takata, K. Domen, *Chem. Mater.* **2009**, *21*, 1543–1549.
[58] H. Li, J. Xiao, J. J. M. Vequizo, T. Hisatomi, M. Nakabayashi, Z. Pan, N. Shibata, A. Yamakata, T. Takata, K. Domen, *ACS Catal.* **2022**, *12*, 10179–10185.
[59] S. Nishimae, J. J. M. Vequizo, Y. Inoue, A. Yamakata, M. Nakabayashi, T. Higashi, K. Domen, *J. Mater. Chem. A* **2023**, *11*, 6299–6310.
[60] T. Higashi, S. Nishimae, Y. Inoue, Y. Kageshima, K. Domen, *ChemPhotoChem* **2023**, *7*, e202300153.
[61] a) X. Wang, H. Huang, M. Zhao, W. Hao, Z. Li, Z. Zou, *J. Phys. Chem. C* **2017**, *121*, 6864–6867; b) A. Ziani, C. Le Paven, L. Le Gendre, F. Marlec, R. Benzerga, F. Tessier, F. Cheviré, M. N. Hedhili, A. T. Garcia-Esparza, S. Melissen, P. Sautet, T. Le Bahers, K. Takanabe, *Chem. Mater.* **2017**, *29*, 3989–3998; c) Y. Zhong, Z. Li, X. Zhao, T. Fang, H. Huang, Q. Qian, X. Chang, P. Wang, S. Yan, Z. Yu, Z. Zou, *Adv. Funct. Mater.* **2016**, *26*, 7156–7163; d) D. Oka, Y. Hirose, H. Kamisaka, T. Fukumura, K. Sasa, S. Ishii, H. Matsuzaki, Y. Sato, Y. Ikuhara, T. Hasegawa, *Sci. Rep.* **2014**, *4*, 4987.
[62] a) J. Fu, S. E. Skrabalak, *Angew. Chem. Int. Ed.* **2017**, *56*, 14169–14173; b) K. Obata, T. Higashi, F. Ye, M. Katayama, K. Takanabe, *ChemPhotoChem* **2023**, *7*, e202200293; c) L. Yang, Q. Fu, L. Wang, J. Yu, X. Xu, *Appl. Catal. B* **2022**, *304*, 120934; d) M. Kodera, Y. Miseki, K. Sayama, *ACS Appl. Energ. Mater.* **2024**, *7*, 675–680.
[63] K. Chen, J. Xiao, J. J. M. Vequizo, T. Hisatomi, Y. Ma, M. Nakabayashi, T. Takata, A. Yamakata, N. Shibata, K. Domen, *J. Am. Chem. Soc.* **2023**, *145*, 3839–3843.
[64] J. Xiao, M. Nakabayashi, T. Hisatomi, J. J. M. Vequizo, W. Li, K. Chen, X. Tao, A. Yamakata, N. Shibata, T. Takata, Y. Inoue, K. Domen, *Nat. Commun.* **2023**, *14*, 8030.
[65] a) A. Kudo, *Int. J. Hydrogen Energy* **2006**, *31*, 197–202; b) M. Liu, Y. Chen, J. Su, J. Shi, X. Wang, L. Guo, *Nat. Energy* **2016**, *1*, 16151; c) Y.-J. Yuan, D. Chen, Z.-T. Yu, Z.-G. Zou, *J. Mater. Chem. A* **2018**, *6*, 11606–11630; d) C. M. Wolff, P. D. Frischmann, M. Schulze, B. J. Bohn, R. Wein, P. Livadas, M. T. Carlson, F. Jäckel, J. Feldmann, F. Würthner, J. K. Stolarczyk, *Nat. Energy* **2018**, *3*, 862–869.
[66] a) A. Ishikawa, T. Takata, T. Matsumura, J. N. Kondo, M. Hara, H. Kobayashi, K. Domen, *J. Phys. Chem. B* **2004**, *108*, 2637–2642; b) A. Ishikawa, T. Takata, J. N. Kondo, M. Hara, H. Kobayashi, K. Domen, *J. Am. Chem. Soc.* **2002**, *124*, 13547–13553; c) H. Yoshida, Z. Pan, R. Shoji, V. Nandal, H. Matsuzaki, K. Seki, L. Lin, M. Kaneko, T. Fukui, K. Yamashita, T. Takata, T. Hisatomi, K. Domen, *Angew. Chem. Int. Ed.* **2023**, *62*, e202312938.
[67] a) V. Nandal, R. Shoji, H. Matsuzaki, A. Furube, L. Lin, T. Hisatomi, M. Kaneko, K. Yamashita, K. Domen, K. Seki, *Nat. Commun.* **2021**, *12*, 7055; b) K. Brlec, C. N. Savory, D. O. Scanlon, *J. Mater. Chem. A* **2023**, *11*, 16776–16787; c) M. Nakabayashi, K. Nishiguchi, X. Liang, T. Hisatomi, T. Takata, T. Tsuchimochi, N. Shibata, K. Domen, S. L. Ten-no, *J. Phys. Chem. C* **2023**, *127*, 7887–7893; d) L. Lin, V. Polliotto, J. J. M. Vequizo, X. Tao, X. Liang, Y. Ma, T. Hisatomi, T. Takata, K. Domen, *ChemPhotoChem* **2022**, *6*, e202200209; e) R. Li, Z. Zha, Y. Zhang, M. Yang, L. Lin, Q. Wang, T. Hisatomi, M. Nakabayashi, N. Shibata, K. Domen, Y. Li, *J. Mater. Chem. A* **2022**, *10*, 24247–24257.
[68] M. Katayama, D. Yokoyama, Y. Maeda, Y. Ozaki, M. Tabata, Y. Matsumoto, A. Ishikawa, J. Kubota, K. Domen, *Mater. Sci. Eng. B* **2010**, *173*, 275–278.
[69] T. Hisatomi, S. Okamura, J. Liu, Y. Shinohara, K. Ueda, T. Higashi, M. Katayama, T. Minegishi, K. Domen, *Energy Environ. Sci.* **2015**, *8*, 3354–3362.
[70] a) H. Yoshida, Z. Pan, R. Shoji, V. Nandal, H. Matsuzaki, K. Seki, T. Hisatomi, K. Domen, *J. Mater. Chem. A* **2022**, *10*, 24552–24560; b) L. Lin, P. Kaewdee, V. Nandal, R. Shoji, H. Matsuzaki, K. Seki, M. Nakabayashi, N. Shibata, X. Tao, X. Liang, Y. Ma, T. Hisatomi, T. Takata, K. Domen, *Angew. Chem. Int. Ed.* **2023**, *62*, e202310607.
[71] L. Lin, M. Nakabayashi, D. Lu, T. Hisatomi, T. Takata, K. Domen, *Chem. Mater.* **2024**, *36*, 1612–1620.
[72] V. Meignen, L. Cario, A. Lafond, Y. Moëlo, C. Guillot-Deudon, A. Meerschaut, *J. Solid State Chem.* **2004**, *177*, 2810–2817.
[73] K. Brlec, S. R. Kavanagh, C. N. Savory, D. O. Scanlon, *ACS Appl. Energ. Mater.* **2022**, *5*, 1992–2001.
[74] a) M. Iwase, M. Nakabayashi, N. Shibata, C. Izawa, M. Katayama, T. Yamada, Y. Inoue, K. Domen, T. Watanabe, *Jpn. J. Appl. Phys.* **2017**, *56*, 055503; b) M. Iwase, M. Nakabayashi, N. Shibata, H. Matsuzaki, H. Kobayashi, T. Yamada, K. Domen, T. Watanabe, *Cryst. Growth Des.* **2019**, *19*, 2419–2427.
[75] T. Hisatomi, T. Yamamoto, Q. Wang, T. Nakanishi, T. Higashi, M. Katayama, T. Minegishi, K. Domen, *Catal. Sci. Technol.* **2018**, *8*, 3918–3925.
[76] G. Ma, J. Liu, T. Hisatomi, T. Minegishi, Y. Moriya, M. Iwase, H. Nishiyama, M. Katayama, T. Yamada, K. Domen, *Chem. Commun.* **2015**, *51*, 4302–4305.
[77] J. Liu, T. Hisatomi, G. Ma, A. Iwanaga, T. Minegishi, Y. Moriya, M. Katayama, J. Kubota, K. Domen, *Energy Environ. Sci.* **2014**, *7*, 2239–2242.
[78] Z. Song, T. Hisatomi, S. Chen, Q. Wang, G. Ma, S. Li, X. Zhu, S. Sun, K. Domen, *ChemSusChem* **2019**, *12*, 1906–1910.
[79] a) M. Cai, X. Wang, J. Xue, Y. Jiang, Y. Wei, Q. Cheng, J. Chen, S. Sun, *Appl. Phys. Lett.* **2021**, *119*; b) M. Yu, S. Grasso, R. Mckinnon, T. Saunders, M. J. Reece, *Adv. Appl. Ceram.* **2017**, *116*, 24–60; c) R. Raj, A. Kulkarni, J.-M. Lebrun, S. Jha, *MRS Bull.* **2021**, *46*, 36–43.
[80] Z. Pan, Q. Xiao, S. Chen, Z. Wang, L. Lin, M. Nakabayashi, N. Shibata, T. Takata, T. Hisatomi, K. Domen, *J. Catal.* **2021**, *399*, 230–236.
[81] X. Wang, Z. Pan, J. J. M. Vequizo, T. Hisatomi, S. Nandy, T. Higashi, L. Lin, J. Xiao, T. Takata, A. Yamakata, W. Yan, K. Domen, *Chem. Commun.* **2023**, *59*, 6913–6916.
[82] a) S. Sun, T. Hisatomi, Q. Wang, S. Chen, G. Ma, J. Liu, S. Nandy, T. Minegishi, M. Katayama, K. Domen, *ACS Catal.* **2018**, *8*, 1690–1696; b) S. Chen, S. Nandy, J. J. M. Vequizo, T. Hisatomi, M. Nakabayashi, Z. Pan, Q. Xiao, Z. Wang, L. Lin, S. Sun, K. Kato, A. Yamakata, N. Shibata, T. Takata, F. Zhang, K. Domen, *ACS Catal.* **2023**, *13*, 3285–3294.
[83] S. Nandy, T. Hisatomi, M. Nakabayashi, H. Li, X. Wang, N. Shibata, T. Takata, K. Domen, *Joule* **2023**, *7*, 1641–1651.
[84] a) K. Seki, T. Higashi, Y. Kawase, K. Takanabe, K. Domen, *J. Phys. Chem. Lett.* **2022**, *13*, 10356–10363; b) K. Wakishima, T. Higashi, A. Nagaoka, K. Yoshino, *New J. Chem.* **2024**, *48*, 131–143; c) S. Chen, D. Huang, P. Xu, W. Xue, L. Lei, M. Cheng, R. Wang, X. Liu, R. Deng, *J. Mater. Chem. A* **2020**, *8*, 2286–2322.
[85] T. Higashi, Y. Shinohara, A. Ohnishi, J. Liu, K. Ueda, S. Okamura, T. Hisatomi, M. Katayama, H. Nishiyama, T. Yamada, T. Minegishi, K. Domen, *ChemPhotoChem* **2017**, *1*, 167–172.
[86] J. Liu, T. Hisatomi, D. H. K. Murthy, M. Zhong, M. Nakabayashi, T. Higashi, Y. Suzuki, H. Matsuzaki, K. Seki, A. Furube, N. Shibata, M. Katayama, T. Minegishi, K. Domen, *J. Phys. Chem. Lett.* **2017**, *8*, 375–379.
[87] Z. Pan, R. Yanagi, T. Higashi, Y. Pihosh, S. Hu, K. Katayama, *Sustain. Energy Fuels* **2022**, *6*, 2067–2074.
[88] T. Higashi, Y. Sasaki, Y. Kawase, H. Nishiyama, M. Katayama, K. Takanabe, K. Domen, *Catalysts* **2021**, *11*, 584.
[89] a) J. Ma, T. J. Miao, J. Tang, *Chem. Soc. Rev.* **2022**, *51*, 5777–5794; b) K. Iwata, T. Takaya, H.-o. Hamaguchi, A. Yamakata, T.-a. Ishibashi, H. Onishi, H. Kuroda, *J. Phys. Chem. B* **2004**, *108*, 20233–20239.
[90] R. Chen, D. Zhang, Z. Wang, D. Li, L. Zhang, X. Wang, F. Fan, C. Li, *J. Am. Chem. Soc.* **2023**, *145*, 4667–4674.

© 2024 The Authors. ChemSusChem published by Wiley-VCH GmbH

18645564x, 2024, 21, Downloaded from https://chemistry-europe.onlinelibrary.wiley.com/doi/10.1002/cssc.202400663 by Turkey Cochrane Evidence Aid, Wiley Online Library on [04/09/2026]. See the Terms and Conditions (https://onlinelibrary.wiley.com/terms-and-conditions) on Wiley Online Library for rules of use; OA articles are governed by the applicable Creative Commons License

[91] a) C. Mu, C. Lv, X. Meng, J. Sun, Z. Tong, K. Huang, *Adv. Mater. Interfaces* **2023**, *10*, 2201842; b) N. Zhang, Y. Xiong, *Curr. Opin. Green Sustain. Chem.* **2023**, *41*, 100796; c) L. Zhang, R. Long, Y. Zhang, D. Duan, Y. Xiong, Y. Zhang, Y. Bi, *Angew. Chem. Int. Ed.* **2020**, *59*, 6224–6229.
[92] A. Talebian-Kiakalaieh, M. Guo, E. M. Hashem, B. Xia, Y. Jiang, C. Chuah, Y. Tang, P. Kwong, J. Ran, S.-Z. Qiao, *Adv. Energy Mater.* **2023**, *13*, 2301594.
[93] Ø. Dahl, M. F. Sunding, V. Killi, I.-H. Svenum, M. Grandcolas, M. Andreassen, O. Nilsen, A. Thøgersen, I. J. T. Jensen, A. Chatzitakis, *ACS Catal.* **2023**, *13*, 11762–11770.
[94] T. Sagara, Y. Aikawa, M. Sukigara, *J. Phys. Chem.* **1987**, *91*, 1173–1177.
[95] F. Lin, S. W. Boettcher, *Nat. Mater.* **2014**, *13*, 81–86.
[96] a) M. R. Nellist, F. A. L. Laskowski, J. Qiu, H. Hajibabaei, K. Sivula, T. W. Hamann, S. W. Boettcher, *Nat. Energy* **2018**, *3*, 46–52; b) F. A. L. Laskowski, S. Z. Oener, M. R. Nellist, A. M. Gordon, D. C. Bain, J. L. Fehrs, S. W. Boettcher, *Nat. Mater.* **2020**, *19*, 69–76; c) S. Daemi, A. Kundmann, K. Becker, P. Cendula, F. E. Osterloh, *Energy Environ. Sci.* **2023**, *16*, 4530–4538; d) B. Dong, J. Cui, Y. Gao, Y. Qi, F. Zhang, C. Li, *Adv. Mater.* **2019**, *31*, 1808185.
[97] a) M. Ebihara, T. Ikeda, S. Okunaka, H. Tokudome, K. Domen, K. Katayama, *Nat. Commun.* **2021**, *12*, 3716; b) R. Chen, F. Fan, C. Li, *Angew. Chem. Int. Ed.* **2022**, *61*, e202117567; c) R. Chen, Z. Ren, Y. Liang, G. Zhang, T. Dittrich, R. Liu, Y. Liu, Y. Zhao, S. Pang, H. An, C. Ni, P. Zhou, K. Han, F. Fan, C. Li, *Nature* **2022**, *610*, 296–301.

Manuscript received: March 27, 2024
Revised manuscript received: May 20, 2024
Accepted manuscript online: May 24, 2024
Version of record online: July 8, 2024

© 2024 The Authors. ChemSusChem published by Wiley-VCH GmbH

18645564x, 2024, 21, Downloaded from https://chemistry-europe.onlinelibrary.wiley.com/doi/10.1002/cssc.202400663 by Turkey Cochrane Evidence Aid, Wiley Online Library on [04/09/2026]. See the Terms and Conditions (https://onlinelibrary.wiley.com/terms-and-conditions) on Wiley Online Library for rules of use; OA articles are governed by the applicable Creative Commons License